10

Continuum mechanics modeling of hydrogen embrittlement

M. R. BEGLEY, University of California Santa Barbara, USA,
J. A. BEGLEY, TCA Solutions, USA and
C. M. LANDIS, The University of Texas at Austin, USA

Abstract: This chapter provides material scientists with essential continuum mechanics concepts and theoretical predictions for the stresses and deformation near cracks, dislocations and inclusions. Detailed summaries of classical crack tip continuum solutions are provided, including elastic fields, small deformation elastic-plastic (HRR) fields, large deformation (blunting) fields, and fields associated with steady-state growing cracks. The results emphasize the relationships between crack tip stresses and loading, yield stress and strain hardening parameters, and enable straightforward estimates of the magnitudes and length-scales over which elevated stresses are present. These estimates can be coupled with physical descriptions of various cracking mechanisms described elsewhere in this book. Solutions are also presented for the stresses surrounding elementary configurations of dislocations and inclusions, to enable estimates of hydrogen uptake near such features.

Key words: continuum mechanics, crack tip fields, fracture parameters, dislocations, inclusions.

10.1 Introduction

The purpose of this chapter is to provide materials scientists with essential continuum mechanics concepts and predictions that provide the basis to understand stress and deformation near cracks, dislocations and inclusions. Rather than focus on the multi-physics simulations enabled by advanced computational frameworks (including those that incorporate descriptions of complex microstructure), the emphasis is on classical results describing deformation and stresses for homogeneous, isotropic materials. These solutions inevitably serve as an effective starting point to estimate (1) the various physical length scales associated with the fracture process zone and (2) the associated stress/deformation magnitudes that drive various cracking mechanisms. Such estimates are critical not only to establishing a global view of failure, but also to identifying the features and assumptions that should be integrated in more detailed simulations that define specific microstructure features.

With this in mind, the reader should be constantly aware that this brief

summary sidesteps the rapidly growing body of literature that examines the interaction of cracks with different microstructural features. Notable examples include single crystal plasticity [1, 2], interactions between cracks, particles, voids and dislocations [2, 3], and discrete dislocation simulations of crack tip behaviors [4–6]. In a similar vein, this overview provides only a brief commentary on cohesive zone modeling of growing cracks, as the formulation and application require multi-physics descriptions that extend beyond plasticity theory. The present chapter is intended as an 'entry point' to this body of literature: the solutions described here can be used to identify the relevant length-scales and stresses defining the fracture process zone for a given set of properties and loading parameters. These results can then be used to identify the subset of discrete feature modeling or cohesive zone formulations that are relevant to a specific scenario.

For isotropic continuum descriptions of fracture, there are two fundamental questions that arise, which both relate to the scale of deformation relative to the geometry of the component and the fracture process zone. The answers to these questions determine the relevant degree of detail (or underlying assumptions) that should be included in the continuum description of fracture. These questions are:

- How large is the fracture process zone associated with inelastic material response in comparison to specimen/component dimensions? The answer to this question determines whether or not the fracture process can be modeled using small-scale yielding approaches, wherein asymptotic elastic boundary conditions are prescribed on the exterior of a domain.
- How large is the region affected by finite deformation (typically taken as the opening of a blunted crack) in comparison to the plastic zone size or component? The answer to this question determines whether or not the details of large deformation near the blunting crack tip are pertinent to the fracture process.

Figure 10.1 provides a graphical representation of these fundamental questions, by illustrating the regions dominated by elastic deformation, plastic deformation and crack tip blunting effects (i.e. finite deformation). In general, for plastic zones that are small relative to the component size, the crack tip fields transition from a far-field elastic solution (with stress scaling as $r^{-1/2}$), to a plastic-solution (with stress scaling as $r^{-n/(n+1)}$ where n is the strain hardening exponent), to a blunted crack solution where the stress peaks then decreases toward the crack tip. One of the principal goals of this chapter is to identify scaling relationships that define the various length-scales illustrated in Fig. 10.1 in terms of geometry and loading parameters: these relationships enable one to identify the appropriate continuum theory to interpret behavior in the fracture process zone.
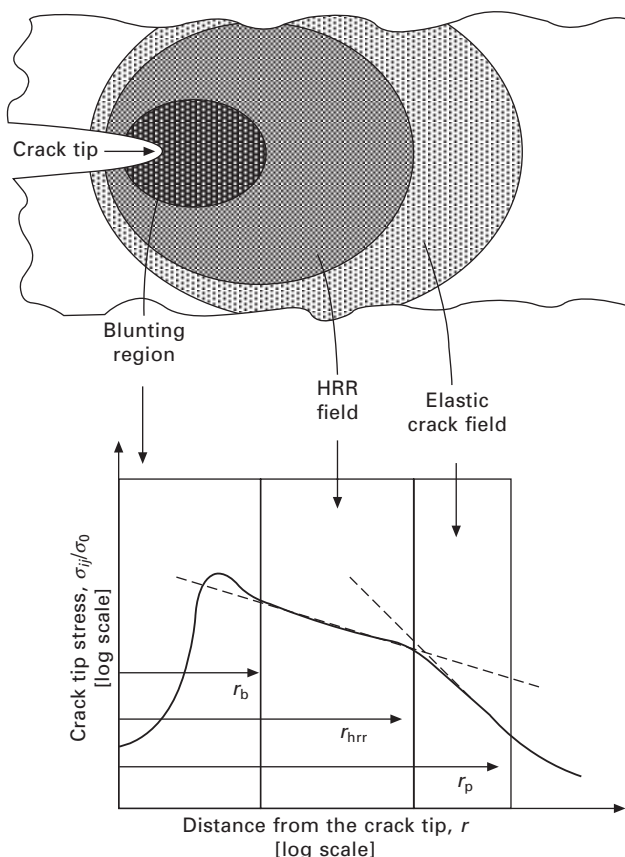
10.1 Schematic illustration of various regions of the crack tip, and associated crack tip length scales. The blunting region is associated with large deformation plastic flow [7]; the HRR region is associated with small deformation plastic flow [8, 9]; the elastic region exhibits the classical $1/\sqrt{r}$ singularity with amplitudes defined by the crack tip stress intensity factor.

Such estimates of the stresses and deformation near crack tips play a critical role in the development of hydrogen cracking models, by providing the basis to quantify the degree and extent of hydrogen uptake near crack tips. As is elucidated in other chapters throughout this book, many embrittlement mechanisms depend strongly on local concentrations of hydrogen, and hydrogen uptake is strongly stress dependent. Therefore, estimates of crack tip stresses serve as a foundation on which a multitude of mechanistic hydrogen cracking models rest. Specific examples of this (i.e. how crack tip fields are coupled to hydrogen cracking models) are provided both in the literature (see ref. [10] for a lucid review) and in Chapter 11.

10.2   Basic concepts

10.2.1 A brief overview of the choices involved in continuum mechanics analyses

There are three essential pieces to any continuum mechanics analysis: (i) a kinematic description of the relationship between strains and displacements, (ii) a constitutive description for the material that relates stresses and strains, and (iii) a statement of equilibrium (alternatively, the principle of virtual work or similar work/momentum conservation statement). There are numerous excellent texts that elucidate how these three mathematical pieces are combined to produce a set of equations that can be solved to determine the stresses, strains and displacements throughout the defined geometry. One of our favorite tomes (comprehensive but still lucid) is Bower [8]. Here, we present only a brief outline of a select set of concepts and approximations that serve as the foundation to interpret results presented in subsequent sections. Only the first two of the essential pieces create the possibility of choice(s) by the analyst: the statement of kinematics (strain–displacement relationships) and the constitutive description (stress–strain relationships).

The choice of kinematic description determines whether or not the problem is solved in terms of 'small deformation' or 'large deformation'. In small deformation, it is assumed that the displacement gradients are small in comparison to unity: this leads to a linear set of differential equations defining strains in terms of displacement gradients. Small deformation analyses are generally the default choice in computational codes for the simple reason that for stiff materials, the deformed geometry is quite similar to the original geometry. Hence, for small deformation analyses, no distinction is made between the original and deformed position of material points. This implies that there is no distinction between stresses referred to the original shape and those referred to the deformed shape.

An obvious, notable and particularly relevant exception to the rule that deformations are generally small for stiff materials is the scenario of an initially sharp crack that experiences blunting, i.e. large geometry changes relative to an initially sharp geometry. In these scenarios, deformation gradients are large, and one must invoke a large deformation definition of strain, and reference the stresses to the deformed shape. In large deformation simulations (also referred to as finite deformation), the deformed position of the material points is taken to be different from their original position. This leads to non-linear differential equations relating strains to displacement gradients, and requires that distinction must be made between stresses referred to the original shape and those referred to the deformed shape. It should be emphasized that large deformation analyses are inherently non-linear, regardless of the material description, and hence are more expensive (computationally) than their small deformation brethren.

Though the deformation near blunting crack tips is invariably large, this does not imply that finite deformation analyses are a 'must': the region of large displacement gradients may be confined to a local region near the crack tip that does not play a significant role in the fracture process zone. As a rule of thumb, the size of the region affected by finite deformation scales with the predicted crack opening displacement (to be defined). For a range of properties and loads, this region may be small compared with the total plastic zone size or the length-scale associated with microstructural features (e.g. the spacing between particles). Hence, small deformation simulations of crack tips are entirely relevant to some scenarios. Indeed, the well-known asymptotic plastic fields at a crack tip developed independently by Hutchinson [9] and Rice and Rosengren [11] are calculated assuming small deformation.

Finally, it should be noted that there is an additional choice by the analyst (unrelated to fundamental principles), namely the choice of crack tip geometry. In most simulations, and notably those involving the assumption of small deformation, the crack tip is defined as a discrete point. Put another way, the crack tip is defined as a point-wise change in boundary conditions applied along a straight boundary: ahead of the crack tip, the displacements along the symmetry plane are zero, while behind the crack tip, the tractions along the symmetry plane are zero. This is often referred to as a 'sharp crack': in essence, the crack boundary is defined as a mathematical line with infinitesimal thickness. For small deformation analyses, this definition leads to singular stresses at the crack tip: as the solution is refined, the stresses go to infinity as the crack tip is approached. The drawback is that the approach may require computation of the deformation/stresses at vanishingly small scales (depending on the tip radius) that may be irrelevant to fracture. The alternative (to the sharp crack geometry) is to define a small radius at the crack tip, such that the crack is defined not as a line but as a slit with finite thickness and rounded ends. In this case, the stresses near the tip radius will be finite: this is the most common approach when solving finite deformation problems.

10.2.2 Constitutive descriptions

Here, attention is limited to isotropic material response: the predominant descriptions used for fracture analyses are linearly elastic, deformation theory plasticity, and flow theory plasticity. These are summarized here to provide a quick reference for describing and interpreting results presented later.

Linear elasticity

Isotropic linear elasticity in three dimensions requires only two elastic constants: the constitutive law is commonly written as:

$$\varepsilon_{ij} = \frac{1+v}{E} \sigma_{ij} + \sigma_{kk}\delta_{ij} + \alpha \Delta T \delta_{ij}$$ [10.1a]

or, conversely:

$$\sigma_{ij} = \frac{E}{1+v}\left(\varepsilon_{ij} + \frac{v}{1-2v}\varepsilon_{kk}\delta_{ij}\right) + \frac{E}{1-2v}\alpha \Delta T \delta_{ij}$$ [10.1b]

where δ_{ij} is the Kronecker delta (i.e. equal to unity for $i=j$ and zero otherwise), E is the elastic modulus of the material, v is the Poisson ratio, α is an isotropic coefficient of thermal expansion, and ΔT is the change in temperature (from a strain-free reference temperature). Note that: (i) in these definitions, the repeated index convention holds (such that $\sigma_{kk} = \sigma_{11} + \sigma_{22} + \sigma_{33}$), and (ii) the strain is defined as the total strain, i.e. the strains generated by stress plus those generated by temperature changes. The mechanical strains are those that lead to the generation of stress, and are represented by the first two terms of equation (10.1a). For example, if a thin film is bonded to a semi-infinite substrate and the substrate's temperature is changed, the total strain in the film is equal to that of the substrate arising from temperature and the stress in the film computed via eqn. (10.1a) scale with the difference in coefficient of thermal expansion (CTE) between the film and substrate.

Deformation plasticity

Many continuum analyses of fracture invoke 'deformation plasticity', which is essentially a non-linear elasticity (hypoelasticity) theory that typically utilizes small strain definitions: the rationale for using hypoelasticity theory is that under monotonically increasing loads, the stresses near a crack do not experience significant unloading. This form of constitutive law was used to develop the HRR fields (i.e. the asymptotic stress/strain distributions in the plastic zone near a sharp crack [9, 11]). The non-linear stress–strain curve from a monotonic uniaxial tension test is used to identify a strain hardening exponent and yield stress by fitting to a functional form that is then used to define the a strain energy function.

The equations below summarize a typical definition of this type of material response: in the following, $\varepsilon_o = \sigma_o/E$ and n are the fitting parameters.

Uniaxial and pure shear responses:

$$\varepsilon = \frac{3(1-2v)}{E}\sigma + \frac{2}{\sqrt{3}}\varepsilon_o\left(\frac{\sigma}{\sigma_o}\right)^n \quad \text{and} \quad \gamma = 2\varepsilon_o\left(\frac{\tau}{\sigma_o}\right)^n$$ [10.2a]

Full stress–strain response:

$$\varepsilon_{ij} = \frac{9(1-2v)}{E}\sigma_H\delta_{ij} + \varepsilon_o\left(\frac{J_2}{\sigma_o}\right)^{n-1}\left(\frac{\sigma_{ij} - \sigma_H\delta_{ij}}{\sigma_o}\right)$$ [10.2b]

Strain energy potential:

$$W(\varepsilon_{ij}) = \frac{E\varepsilon_{\mathrm{m}}^2}{18\,(1-2v)} + \frac{2n\sigma_{\mathrm{o}}\varepsilon_{\mathrm{o}}}{n+1}\left(\frac{\varepsilon_{ij}\varepsilon_{ij} - \frac{1}{3}\varepsilon_{\mathrm{m}}^2}{2\varepsilon_{\mathrm{o}}^2}\right)^{\frac{n+1}{2n}}$$

[10.2c]

Here, $\sigma_{\mathrm{H}} = \sigma_{kk}/3$ is the hydrostatic stress, $\varepsilon_{\mathrm{m}} = \varepsilon_{kk}$ is the dilatation strain, and $J_2 = \sqrt{\frac{1}{2}(\sigma_{ij}\sigma_{ij} - 3\sigma_{\mathrm{H}}^2)}$ is the second invariant of the stress tensor. Because the non-linear portion of the response is expressed in terms of the second stress invariant, this theory is sometimes referred to as J_2 deformation theory.

J_2 flow theory

By far, the greatest number of computational continuum simulations adopt this path-dependent, rate-independent description of material response, which is also commonly referred to as 'incremental plasticity'. The distinction with deformation plasticity is that the material will unload elastically when the stresses decrease from a previously elevated level regardless of prior inelastic loading. Here, attention is limited to isotropic materials with power-law hardening. The formulation involves solving for stress or strain increments associated with an incremental change in external loading conditions (which may involve either prescribed tractions or displacements). The model takes its name from its use of the second stress invariant as the sole quantity dictating whether or not plastic deformation occurs. Whether or not the material experiences yielding is determined by the condition:

$$\sigma_{\mathrm{e}} = \sqrt{\frac{3}{2}s_{ij}s_{ij}} \geq \blacksquare(\varepsilon_{\mathrm{P}})$$

[10.3a]

where σ_{e} is an effective stress measure defined in terms of the deviatoric stresses $\sigma_{ij} = \sigma_{ij} - \sigma_{\mathrm{H}}\delta_{ij}$. The quantity ε_{P} is a scalar measure of the effective plastic strain, which is determined by the summation (integration) of all plastic strain increments calculated via previous load increments:

$$\varepsilon_{\mathrm{P}} = \int \sqrt{\frac{2}{3}\mathrm{d}\varepsilon_{ij}^{\mathrm{P}}\,\mathrm{d}\varepsilon_{ij}^{\mathrm{P}}}\ \mathrm{d}t$$

[10.3b]

where t represents a fictitious time corresponding to the history of loading. The yield function, $Y(\varepsilon_{\mathrm{P}})$, is determined via empirical fits to the measured uniaxial response of the material that plots stress versus plastic strain. With these definitions, here is the complete set of equations defining the material response (see ref. [8] for complete details):

$$\mathrm{d}\varepsilon_{ij} = \mathrm{d}\varepsilon_{ij}^{\mathrm{e}} + \mathrm{d}\varepsilon_{ij}^{\mathrm{P}}$$

[10.3c]

$$d\varepsilon_{ij}^e = \frac{1+v}{E}d\sigma_{ij} - \frac{v}{E}d\sigma_H\delta_{ij}$$ [10.3d]

$$d\varepsilon_{ij}^P = \begin{cases} 0 & \sigma_e < Y(\varepsilon_P) \\ \dfrac{9s_{ij}s_{kl}d\sigma_{kl}}{4h[Y(\varepsilon_P)]^2} & \sigma_e = Y(\varepsilon_P) \end{cases}$$ [10.3e]

where $h = dY/d\varepsilon_P$ is the hardening modulus, and it should be understood that the plastic strain increments are zero whenever $s_{kl}d\sigma_{kl} \le 0$. For uniaxial tension, the above equations return the expression $\sigma_f = Y(\varepsilon_P)$ for stresses that cause plastic yielding. A typical form (including that adopted for the results presented in the next section) is $\varepsilon_P = \varepsilon_o(Y/\sigma_o)^n - Y/E$. In this case, $n = \infty$ corresponds to an elastic, perfectly plastic material that has no hardening.

10.2.3 Fundamental definitions of fracture parameters

The stability of cracks is determined by one of three loading parameters that characterize the state of stress (or deformation) ahead of the crack tip: K, G and J. These loading parameters depend on the crack geometry and applied loads, and (for the most part) fully define the crack tip stress and deformation fields.

For monotonically increasing loading (at rates large enough to neglect creep, oxidation, etc.), rapid crack advance occurs when the loading parameter reaches the critical value for the material, K_{IC}, G_C or J_C referred to here generically as the toughness. When a crack slowly advances at a loading parameter beneath that which causes instantaneous crack growth, 'subcritical' growth is said to occur. Typically, there is a critical value of the loading parameter needed to cause subcritical growth (at some arbitrarily defined measurable rate), commonly referred to as the 'threshold' growth parameter, e.g. K_{th}. Many instances of hydrogen-assisted cracking are classic examples of sub-critical crack growth: even though the loading parameter (K, G or J) is far below the value needed to drive rapid crack growth, crack growth nonetheless occurs, albeit more slowly. Care should be taken to distinguish between hydrogen effects that impact the threshold loading parameter for slow growth (material property), or those that impact the critical loading parameter for fast growth (a separate material property). The former are far more prevalent than the later.

The stress intensity factor (SIF) is defined by the amplitude of the asymptotic elastic stress field ahead of the crack, which exhibits a characteristic singularity. In general, the stress distribution close to the tip of a crack can be written (for polar coordinates) as:

$$\sigma_{ij} = \frac{K_{\mathrm{I}}}{\sqrt{2\pi r}}\, f_{ij}^{\mathrm{I}}(\theta) + \frac{K_{\mathrm{II}}}{\sqrt{2\pi r}}\, f_{ij}^{\mathrm{II}}(\theta) + \frac{K_{\mathrm{III}}}{\sqrt{2\pi r}}\, f_{ij}^{\mathrm{III}}(\theta) \qquad [10.4]$$

where the subscripts I, II and III refer to different modes of loading: mode I – opening, mode II – in-plane shear, and mode III – anti-plane shear (tearing). The functions f_{ij}^{Q} (Q = I, II, III) are dimensionless functions of the angular position from the direction of crack propagation. In this chapter, we limit our attention to cracks loaded in mode I. The SIF also dictates the crack face displacements near the tip (see Section 10.3.1).

The stress intensity factors are determined by solution to an elasticity problem with a sharp crack: they are defined by the loads applied to the structure and the crack length or other length-scale in the problem.

For instantaneous crack growth, critical loads/crack lengths correspond to the condition that (for mode I, for example) $K_{\mathrm{I}} = K_{\mathrm{IC}}$, where K_{IC} is the material's toughness. As mentioned above, there are instances in which cracks will advance slowly at levels of applied stress intensity factor that are beneath the material toughness. This is often referred to as sub-critical crack growth, and is typically characterized by the condition $K_{\mathrm{IC}} > K_{\mathrm{I}} > K_{\mathrm{th}}$: that is, for sub-critical crack growth the applied stress intensity factor must be below the value that leads to instantaneous growth and above a threshold value (a material and potentially environmentally specific property), below which no crack advance occurs.

The energy release rate (ERR) is the defined as the change in mechanical energy during infinitesimal crack advance, defined by per unit area. For planar problems, with a domain defined by thickness b and the crack length a, the energy release rate is defined as:

$$G = -\frac{\partial U_{\mathrm{m}}}{\partial A} = \frac{1}{b}\frac{\partial U_{\mathrm{m}}}{\partial a} \qquad [10.5]$$

where U_{m} is the potential energy of the system and the crack surface area is $A = b \cdot a$. Like the SIF, the energy release rate is determined by solution to an elasticity problem with a sharp crack, and is defined by the loads and geometry. Instantaneous failure occurs when $G = G_{\mathrm{C}}$, where G_{C} is the critical energy release rate for the material (or interface). Again, sub-critical crack growth (defined above) may occur for loading parameters that are in the range: $G_{\mathrm{C}} > G > G_{\mathrm{th}}$.

Since G and K are defined for an elastic material, there is a simple relationship between them, known as via Irwin's relation. For pure mode I,

$$G = \frac{K_{\mathrm{I}}^{2}}{\overline{E}} \qquad [10.6]$$

where $\overline{E} = E$ for plane stress, and $\overline{E} = E/(1 - v^2)$ for plane strain deformation. For scenarios where the size of the plastic zone (discussed in what follows)

are small compared with other length-scales, the same relationship holds between G_C and K_{IC}, and/or G_{th} and K_{th}, i.e. the critical values for instaneous and sub-critical crack growth, respectively.

The final fracture parameter is determined via a contour integral known as the J-integral. For a crack aligned with the x_1 axis, propagating the same direction, the J-integral is defined as [11]:

$$ J = \oint_\Gamma \quad \mathrm{d}x_2 - \bar{t} \cdot \frac{\partial \bar{u}}{\partial x_1}\, \mathrm{d}s \qquad\qquad [10.7] $$

where Γ is a closed contour surrounding the crack tip, W is the strain energy density, $\bar{t}$ is the traction vector acting on the contour, and $\bar{u}$ is the displacement along the contour. For linear elastic materials, $J = G$. For purely elastic materials, even non-linear ones (such as deformation plasticity), J is independent of the path chosen. For plastic materials (such as J_2 flow theory), when the integral evaluated along contours that experience purely proportional loading (such that all stresses increase in constant proportion to another), J is independent of the path chosen. For monotonically loaded cracks in plastic materials, the stresses in the plastic zone are *nearly* proportional, such that J is *approximately* path-independent. The seminal works by Hutchinson [9] and Gangloff [10] illustrate that J controls the amplitude of the asymptotic plastic fields, known as the HRR fields. Hence, J is the relevant parameter for predicting failure for ductile materials.

It is worth emphasizing that the critical values of the loading parameters (G, K or J) that indicate the onset of instantaneous cracking or sub-critical growth can depend strongly on the time history of loading/crack growth, and current environmental conditions. For example, in many ductile materials, the critical value of J that is needed to advance the crack depends on the crack length itself, with increasing values of J needed to continue crack propagation. This is known as 'resistance curve' behavior, or 'R-curve behavior': the critical value of G, K or J that is needed to first initiate crack growth is known as the initiation toughness. The critical parameter increases with crack length until it plateaus at a value that does not change with subsequent advances, often referred to as the steady-state toughness. The slope of the toughness vs. crack length curve (which sets the length-scales of crack advance needed to realize higher levels of fracture resistance) is known as the tearing modulus. One of many factors dictating this type of behavior is the difference in crack tip stress distribution and deformation distribution between stationary and propagating cracks, as is discussed in subsequent sections.

The initial increase in toughness due to crack advance (characterized by the tearing modulus), the crack length required to reach the steady-state toughness value, and the magnitude of the increase in toughness over the initiation value has obvious and critical implications for crack stability in service. Even more importantly as far as this book is concerned, the resistance

curve behavior has been shown to be severely degraded by environmental hydrogen and chemically precharged hydrogen, as illustrated in Chapter 8 in Volume 1. Hydrogen can lower the initation toughness and the tearing modulus, with increasing deleterious effects and with increasing hydrogen concentration in the fracture process zone.

10.3 Crack tip fields: asymptotic elastic and plastic solutions

10.3.1 Elastic crack tip fields and stress intensity factors

Detailed treatments of asymptotic elastic crack tip fields (and their derivation) abound (e.g. [8, 12]: this section is meant merely to provide a handy reference for the fields and several important solutions for stress intensity factors. The coordinate system is shown in Fig. 10.2. The asymptotic crack tip fields are summarized below. Note that the stresses are referred to in the x–y coordinate system, but the position is expressed in terms of polar coordinates.
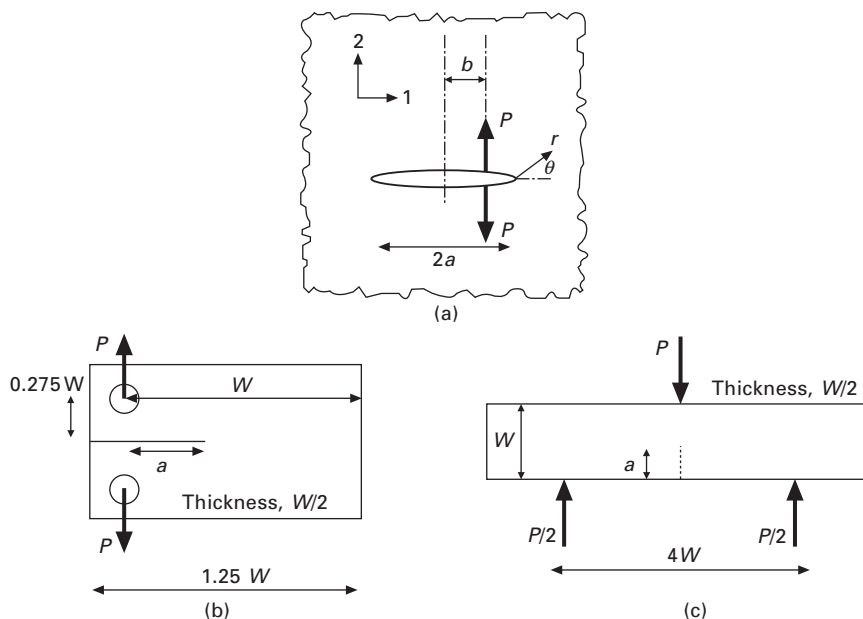
10.2 Schematic illustration of common geometries and loadings used in fracture studies: (a) an isolated crack in a center panel, with point forces acting on the crack face: this scenario can be used to generate a wide variety of solutions via superposition, (b) a compact tension specimen, and (c) a three-point bend specimen. Stress intensity factors for these cases are given in Table 10.1.

Near tip tress components:

$$\sigma_{11} = \frac{K_I}{\sqrt{2\pi r}} \cos \frac{\theta}{2} \left(1 - \sin \frac{\theta}{2} \sin \frac{3\theta}{2}\right) \qquad [10.8a]$$

$$\sigma_{22} = \frac{K_I}{\sqrt{2\pi r}} \cos \frac{\theta}{2} \left(1 + \sin \frac{\theta}{2} \sin \frac{3\theta}{2}\right) \qquad [10.8b]$$

$$\sigma_{12} = \frac{K_I}{\sqrt{2\pi r}} \cos \frac{\theta}{2} \sin \frac{\theta}{2} \cos \frac{3\theta}{2} \qquad [10.8c]$$

Plane strain displacement fields near the tip:

$$u_1 = \frac{2(1+v)K_I}{E} \sqrt{\frac{r}{2\pi}} \cos \frac{\theta}{2} \left(1 - 2v + \sin^2 \frac{\theta}{2}\right) \qquad [10.9a]$$

$$u_2 = \frac{2(1+v)K_I}{E} \sqrt{\frac{r}{2\pi}} \sin \frac{\theta}{2} \left(2 - 2v + \cos^2 \frac{\theta}{2}\right) \qquad [10.9b]$$

Recall that the stress intensity factor K_I is a function of geometry and applied loads, which are determined via solution to the entire elasticity problem for the body containing the crack. Several common geometries are illustrated in Fig. 10.2: the corresponding stress intensity factors are given in Table 10.1 in terms of the specimen geometry and loading.

Table 10.1 Stress intensity factors for three common geometries

|	
Isolated crack with point forces (Fig. 10.2(a))	$K_I\big|_{za} = \dfrac{P}{\sqrt{2a}} \sqrt{\dfrac{a \pm b}{a \mp b}}$
Compact tension specimen (Fig. 10.2(b))	$K_I = \dfrac{P}{B}\sqrt{\dfrac{\pi}{W}} \left\{ 16.7\left(\dfrac{a}{W}\right)^{1/2} - 104.7\left(\dfrac{a}{W}\right)^{3/2} + 369.9\left(\dfrac{a}{W}\right)^{5/2} - 573.8\left(\dfrac{a}{W}\right)^{7/2} + 360.5\left(\dfrac{a}{W}\right)^{9/2} \right\}$
Three-point bend specimen (Fig. 10.2(c))	$K_I = \dfrac{P}{B}\sqrt{\dfrac{\pi}{W}} \left\{ 1.6\left(\dfrac{a}{W}\right)^{1/2} - 2.6\left(\dfrac{a}{W}\right)^{3/2} + 12.3\left(\dfrac{a}{W}\right)^{5/2} - 21.2\left(\dfrac{a}{W}\right)^{7/2} + 21.8\left(\dfrac{a}{W}\right)^{9/2} \right\}$

When stress intensity factors are found via solution to a linearly elastic solution (small deformation and linear elastic material), solutions can be superposed to generate solutions for combined loading. For example, consider an isolated crack subjected to a uniform normal pressure σ on its crack faces: the differential force (per unit thickness of through-cracked body) acting on a small piece of the crack face of width db is d$P = \sigma$db. The solution for the total stress intensity factor due to the distributed pressure is determined by integrating the stress intensity factors resulting from the application of the point forces:

$$K_{\mathrm{I}} = \int_{-a}^{a} \frac{\sigma}{\sqrt{\pi a}} \left(\sqrt{\frac{a+b}{a-b}} \right) \mathrm{d}b = \sigma\sqrt{\pi a} \qquad [10.10]$$

Note that for the point force solution, the signs inside the radical flip for b < 0: however, this is canceled by the fact that the contribution is sought for the crack tip on the opposite side of the point force. This result is identical to that of a stress-free crack of length $2a$ in a panel loaded remotely (at infinity) with the stress σ. Superposition explains this equivalence: the remote tension case is obtained by adding (to the pressurized crack case) the results for a cracked panel with the remote stress σ and a compressive stress σ on the crack faces, which cancels the crack face pressure. Since the applied stress intensity factor for this case is zero, the two stress intensity factors must be equivalent. Similar concepts are applied in the Dugdale model for plastic damage extended from a crack tip (see for example, [12]).

10.3.2 Elementary estimates of plastic and damage zone sizes

The elastic crack tip fields described in the previous section can be used to estimate the size of the near tip region that experiences yielding or elevated hydrostatic stresses. The simplest estimate for the size of the plastic zone near the crack tip is obtained by computing the effective (von Mises) stress (using the asymptotic elastic crack tip fields, given by Equations 10.8 with Equation 10.3a), and setting this equal to a fraction of the yield stress, σ_o. (Typically this fraction is taken as unity.) The result is an equation involving (r, θ) which represents an estimate contour of the plastic zone. Figure 10.3 (left) illustrates Von Mises stress (or effective stress) contours for plane strain, i.e. when $\sigma_{33} = v(\sigma_{11} + \sigma_{22})$ [8]. The stress ahead of any crack tip will scale with the applied SIF: one typically plots contours for distances normalized by the crack length as done in this figure, since this usually sets the length-scale for the problem. Hence, stress contours in $(x/a, y/a)$ space normalized by the quantity $K_{\mathrm{I}}\sqrt{a}$ are universal, in the sense that they are applicable for any crack geometry (provide that one is close to the crack tip such that asymptotic fields are applicable).
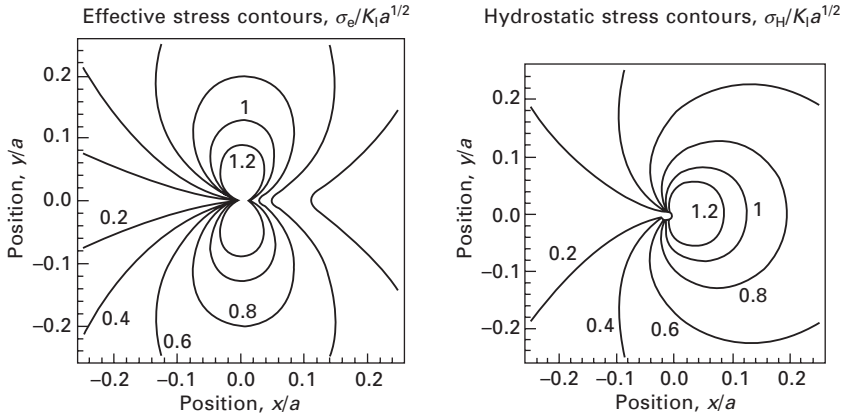
10.3 Contours of effective stress and hydrostatic stress as predicted via elastic crack tip field solutions.

One can solve the (r, θ) equation for the angular position for which the radial distance from the tip is a maximum. This yields:

$$r_\mathrm{p}^\mathrm{max} = \frac{2(1 - v + v^2)^2}{3\pi} \left(\frac{K_\mathrm{I}}{\sigma_\mathrm{o}}\right)^2 \approx \frac{1}{2\pi}\left(\frac{K_\mathrm{I}}{\sigma_\mathrm{o}}\right)^2 \qquad [10.11]$$

The weak dependence on the Poisson ratio is a result of the fact that the angular position corresponding to maximum plastic varies from $\theta = 70°$ for $v = 0$ to $\theta = 90°$ for $v = 1/2$. One can adopt other approximations for the plastic zone size [12]: however, this estimate is generally with 25% of the 'exact' elastic-plastic solution obtained via finite element analysis. (See stress distributions presented in subsequent sections.)

For hydrogen embrittlement, the size of the near tip region that experiences elevated hydrostatic stresses is of central concern to hydrogen induced damage. Suppose that one wants to calculate the size of the region over which $\sigma_\mathrm{H} > n\sigma_\mathrm{o}$, where n is some fraction dictated by scaling considerations associated with hydrogen enhancement in the dilated lattice. The size of the region with elevated hydrostatic stresses is then estimated as:

$$r_\mathrm{H}^\mathrm{el} = \frac{32}{81\pi}\left(\frac{K_\mathrm{I}}{n\sigma_\mathrm{o}}\right)^2 \approx \frac{1}{8}\left(\frac{K_\mathrm{I}}{n\sigma_\mathrm{o}}\right)^2 \qquad [10.12]$$

It should be noted that the maximum dimension is aligned with $\theta = 90°$, regardless of the Poisson ratio. Note that the size of the region over which the hydrostatic stress is equal to or greater than the yield stress (in the direction of maximum elevation) is about 75% of the plastic zone size. It is also worth nothing that large deformation effects (i.e. blunting) and strain hardening will result in much higher hydrostatic stresses in a highly localized region

that is contained within a small fraction of the total plastic zone size. (See subsequent sections.)

10.3.3 Singular plastic crack tip fields: the HRR solutions

Analogous to the results for linearly elastic materials, Hutchinson [9] and Gangloff [10] identified asymptotic singular crack tip fields for materials described by deformation plasticity, which are now referred to as the HRR fields. The HRR fields describe the radial and angular dependence of stresses and deformation near the tip of a stationary sharp crack, assuming small deformation. Here, the results for plane strain are summarized: the HRR solutions assume that the material is incompressible in the plastic zone, such that $\sigma_{zz} = (\sigma_{rr} + \sigma_{\theta\theta})/2$. The uniaxial constitutive response of the material is assumed to be:

$$\frac{\varepsilon}{\varepsilon_o} = \alpha\left(\frac{\sigma}{\sigma_o}\right)^n \qquad [10.13]$$

where $\varepsilon_o = \sigma_o/E$. Note that $n \geq 1$ in this case. The HRR stress fields are described by:

$$\frac{\sigma_{ij}}{\sigma_o} = \left(\frac{EJ}{\alpha\sigma_o^2 I_n r}\right)^{\frac{1}{n+1}} \tilde{\sigma}_{\blacksquare}(n,\theta) \qquad [10.14]$$

where I_n is a dimensionless constant and $\tilde{\sigma}_{ij}(n,\theta)$ are dimensionless angular distribution functions that depend on the hardening exponent. An accurate interpolation function for I_n determined from Hutchinson's results is given by:

$$I_n = 3.6\left(1 + \frac{1}{n^2}\right) \qquad [10.15]$$

This is a least-squares fit to Hutchinson's original data, which has been verified by finite element results presented in subsequent sections. The angular functions are illustrated in Fig. 10.4 for several different values of hardening exponent. This fit has been determined for cases with $3 \leq n \leq 15$, but is likely reasonably accurate for larger n values. Figure 10.5 illustrates contours of the near tip hydrostatic stress distribution. The dimensionless coefficient from Equation 10.14, which determines the maximum hydrostatic stress components normalized by the yield stress σ_o, ahead of the crack tip as a function of angle and hardening exponent is:

$$\tilde{\sigma}_H^{max}(n) = \max\left[\frac{3}{2}[\tilde{\sigma}_{rr}(n,\theta) + \blacksquare_{\blacksquare}(n,\theta)]\right] = 7.14 - 2.5e^{-0.1n} \qquad [10.16a]$$
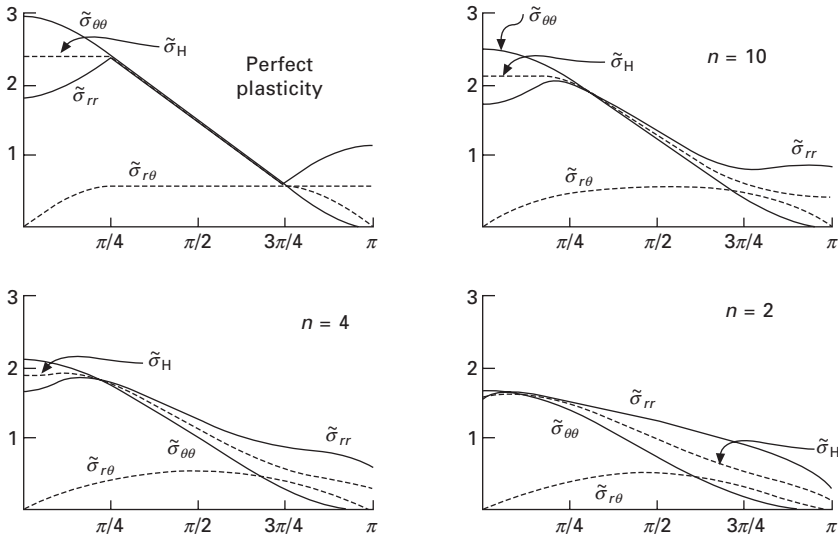
10.4 Angular distribution functions for the stress components predicted by the singular small deformation HRR solutions for plane strain [8, 9]. Note that the HRR solution assumes $\sigma_{zz} = (+\sigma_{\theta\theta})/2$.

Again, this is a numerical fit determined from finite element analysis in the range shown in Fig. 10.5. Similarly, the normalized maximum tensile stress head of the crack can be computed from:

$$\tilde{\sigma}_{\theta\theta}^{\max}(n) = 4.42 - 3.6\,e^{-0.16n^2} \tag{10.16b}$$

which again, is an empirical function determined via fitting to finite element results. The maximum tensile stress is always at $\theta = 0°$, whereas the maximum hydrostatic stress occurs at $\theta = 45°$ for perfectly plastic materials and transitions towards $\theta = 0°$ as the degree of hardening increases (i.e. as n decreases).

In a similar manner the crack tip plastic strain field is expressed as,

$$\frac{\varepsilon_{ij}}{\varepsilon_{\mathrm{o}}} = \blacksquare \left(\frac{EJ}{\alpha\sigma_{\mathrm{o}}^2 I_n r}\right)^{\frac{n}{n+1}} \tilde{\sigma}_{\blacksquare}(n, \theta) \tag{10.17}$$

The path-independent nature of J provides computational advantages. For small-scale yielding, J can be accurately evaluated with recourse to linear elastic stress intensity factors. Additionally the energy interpretation of allows experimental determination of J for linear elastic and elastic-plastic loading conditions (see [12]).

The above presentation emphasizes the direct analogy between linear elastic and plastic crack tip fields. The analogy extends further in the sense
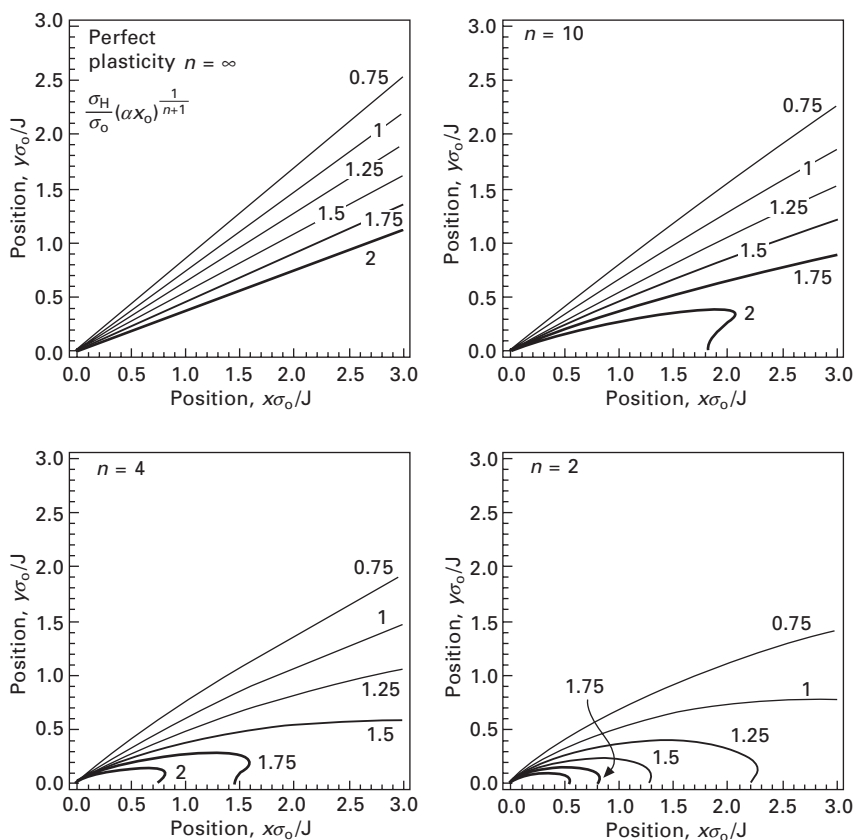
10.5 Contours of hydrostatic stress levels σ_H/σ_o predicted by the small deformation HRR solution [8, 9] for various hardening coefficients. Stresses are normalized by the pre-factor of the asymptotic fields that is left when the scaling $(r\sigma_o/J, \theta)$ is factored out of the HRR solution (see inset on top left).

that both fields are represented by the singular first term of an asymptotic expansion about the crack tip. As discussed later it is sometimes useful to consider additional terms in the both expansion series.

The linear elastic crack tip field is a very good representation of elastic stresses in the vicinity of the crack tip, near the outer edge of the plastic zone: this is often referred to as the *K* zone. In Fig. 10.1, this zone is outside the HRR zone (i.e. where elastic-plastic asymptotic fields are accurate). The region of approximate validity of the *K* zone stresses scales with the crack size. It is also limited by the closeness of in-plane dimensions of the cracked body to the crack tip. For a large body where crack length is the limiting dimension, *K* zone stresses are accurate to 93% at a distance from the crack tip that is 10% of the crack length.

10.4   Crack tip fields: finite deformation blunting predictions

Most often the practical application of a plastic crack tip singular field characterized by J is impacted by the size of the blunted crack tip region. Plastic blunting of a crack tip can be analyzed using a finite deformation large strain approach. Here, the finite deformation generalization of the Prandtl–Reuss equations for the J_2-flow theory of plasticity is used for the multiaxial generalization of the material constitutive response [7, 8, 13]. $Y(\varepsilon_P)$ is a yield function which represents the current level of yield strength, and h is the hardening modulus such that $h = dY/d\varepsilon_P$ (see Section 10.2). Here, the yield function is defined as:

$$\frac{\varepsilon_P}{\varepsilon_o} = \left(\frac{Y}{\sigma_o}\right)^n - \frac{Y}{\sigma_o} \qquad [10.18]$$

The hardening modulus h can be derived as,

$$h = \frac{dY}{d\varepsilon_P} = \frac{\sigma_o}{\varepsilon_o}\frac{1}{n\left(\dfrac{Y}{\sigma_o}\right)^{n-1} - 1} \qquad [10.19]$$

where n is defined as the stress hardening exponent as in Equation 10.18. The study of the crack-tip stresses will take place within the context of the small scale yielding boundary layer approach described in refs [14, 15]. A semi-infinite crack with crack flanks along the negative x-axis and crack tip located at the origin is studied. At sufficiently remote distances from the crack tip, the fields are governed by linear elasticity and the stresses approach the combined asymptotic fields given in Section 10.3. Plane strain conditions are imposed in the out-of-plane direction. In the present simulations, the maximum radial distance from the crack tip to the model perimeter, R, is approximately three times the plastic zone size (as calculated using the results in Section 10.3 based on the initial yield stress σ_o).

The calculation of the fields is carried out by separating the x–y plane into two regions, a small circular region of radius R that must encompass the entire plastic zone and the remainder of the plane composed of linear elastic material. The inner circular region is represented by a finite-element mesh of 9-noded isoparametric elements with 4-point reduced integration for the hydrostatic strains, and full 9-point integration for the deviatoric strains.

The region outside the mesh is represented by a Dirichlet to Neumann map for a semi-infinite crack. The full derivation of these boundary conditions is given in Carka *et al.* [16], who build upon prior work of Givoli and coworkers [17, 18] and Hilton and Hutchinson [19]. The basic idea is that the region outside the mesh adds both stiffness contributions and forces

associated with the K–T field to the boundary of the finite element mesh. (T stresses are defined and discussed in Section 10.4.2.) The finite element connectivity of the infinite region stiffness mimics a super-element with stiffness interactions between each of the degrees of freedom on the outer boundary. Ultimately these boundary conditions allow for a very dense mesh in the plastic zone with no degrees of freedom expended by attempting to model the infinite region with a large but finite domain. Furthermore, no finite size approximation, imposed by applying either traction or displacement boundary conditions at a finite radial distance, is needed to represent the far-field loading since the true infinite boundary conditions are enforced to within the same accuracy as the angular discretization on the outer boundary allows.

Within certain limits, crack tip blunting leads to a unique, stationary, self-similar crack tip plastic field that scales with distance ahead of the crack tip normalized by the crack opening [13]. Here, the initial crack tip is modeled with a small radius: when the applied loading is such that the crack opening displacements are much larger than this radius, the initial notch radius has no effect and the field variables are governed by a self-similar distribution whose length-scale is controlled by the quantity J/σ_0. Hence, one must apply large enough remote loads such that the opening is sufficiently large and self-similarity is obtained. In all but a few simulations corresponding to large amounts of strain hardening (e.g. $n = 0.5$), self-similarity is obtained prior to the interior plastic zone reaching the outer boundary of the imposed asymptotic elastic field.

10.4.1 Crack blunting: large deformation solutions near the crack tip

Figure 10.6 shows plots of stresses directly ahead of a blunted crack tip from a finite deformation large strain analysis. The distance from the crack tip, r, is normalized by the crack opening displacement, δ_t. The crack opening displacement δ_t is defined here as the displacement of the point on the crack face that initially lies at $\theta = 135°$, i.e. the point in the mesh where the straight crack front begins to transition into the initial notch radius. The results in Fig. 10.6 illustrate the transition from the elastic singularity (at large distances) to the HRR solution (at intermediate distances) to a region dominated by finite deformation effects. It is interesting to note that the out-of-plane stresses do not agree with the HRR solution at any point in their distribution: this is because the HRR solution (i) invokes incompressibility through the domain of solution, and (ii) makes the *a priori* assumption that the plastic field surrounds the crack tip. A key implication of this difference is that the HRR fields slightly overestimate the hydrostatic stresses in the HRR-dominated zone.
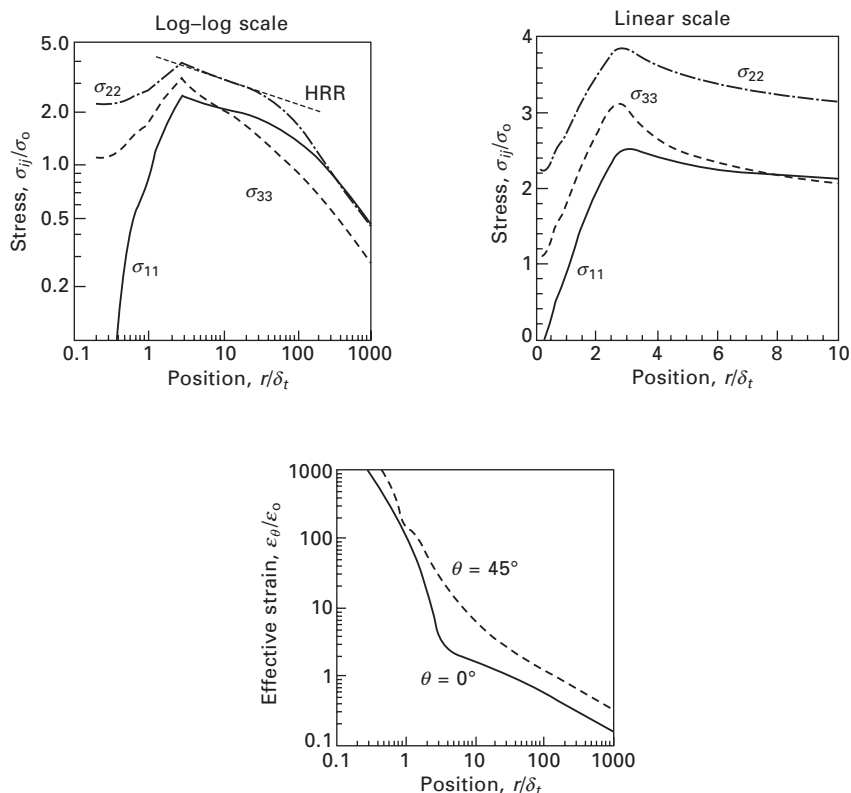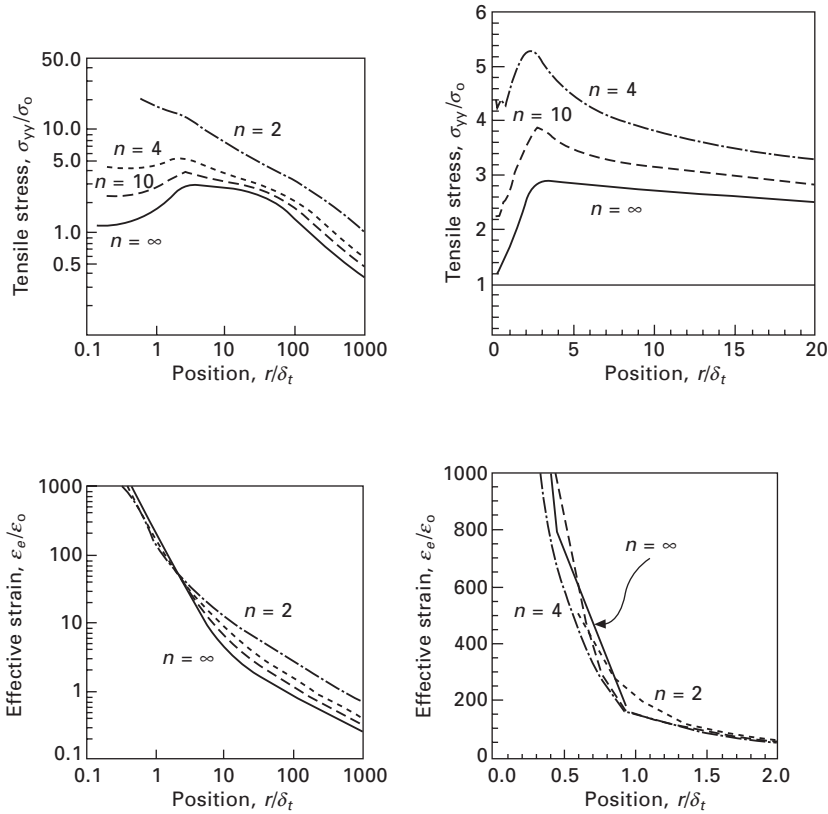
10.6 Large deformation (blunting) predictions for stress and strain distributions near the crack tip, for $n = 10$, $\varepsilon_0 = 0.002$: stresses are shown on log–log scale to illustrate the power-law dependence suggested by the HRR fields. They are also shown on a linear scale (top right) to illustrate elevated stresses are maintained over significant distances. Note that $\sigma_{33} \neq (\sigma_n + \sigma_{22})/2$ as assumed by the HRR solutions (except in the blunting region). The bottom shows effective total strain distributions at two orientations, illustrating the maximum effective strains are experienced along a ray emanating at 45° from the crack tip.

These results are self-similar, in that the length-scale is dictated by J/σ_0. As loading increases the magnitudes of the stresses remain essentially constant for a given value of rJ/σ_0. The load increase only serves to increase $\delta_t = f(n, \varepsilon_0)J/\sigma_0$, which sets the length scale over which high stresses occur. The dimensionless pre-factor in this equation is defined in the next subsection. In contrast to small deformation assumptions where all stresses are singular at the crack tip, the normal stress, σ_{11}, parallel to the crack must be zero at the crack tip free surface. This stress then increases with distance ahead of the crack tip. The buildup of triaxiality ahead of the crack tip peaks at r

$\approx (2 - 3)\,\delta_t$. This leads to a peak stress normal to the crack plane, σ_{22}, and a peak in the tensile hydrostatic pressure, σ_H, at the same position. Near peak stresses are maintained over a distance on the order of δ_t in both the x and y directions. Stresses normal to other radial lines from the crack tip are less than the $\theta = 0°$ line.

The crack opening also sets the length-scale for high strain regions. Figure 10.6 also shows plots of effective strain versus r/δ_t. Strains rapidly decrease from the crack tip out to about $r/\delta_t = 2$. Note that $\varepsilon_e/\varepsilon_o = 10^3$ is roughly a strain of 200%. The highest effective strains occur along a radial line at $\theta = 45°$, instead of directly ahead of the crack.

For a given yield strength, peak normal stresses increase as the strain hardening exponent (denoted as n and defined in Equation 10.18) increases. This is illustrated in Fig. 10.7. Figure 10.8 shows the same effect for hydrostatic stress. Strain hardening has a lesser effect on the location of peak stresses

10.7 Large deformation (blunting) predictions for tensile stresses and effective strains near the crack tip for several different stress hardening exponents, shown on different scales. Results are for $\varepsilon_o = 0.002$.
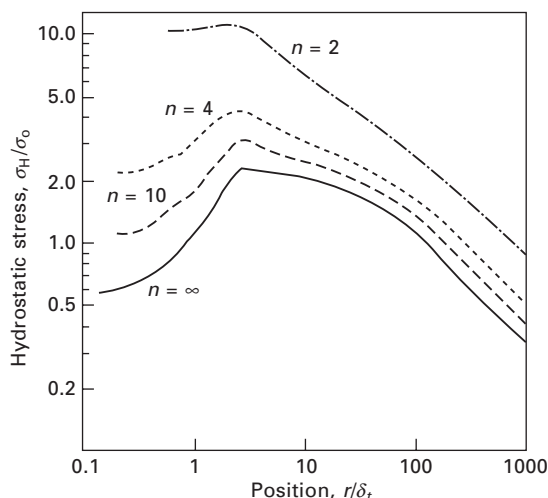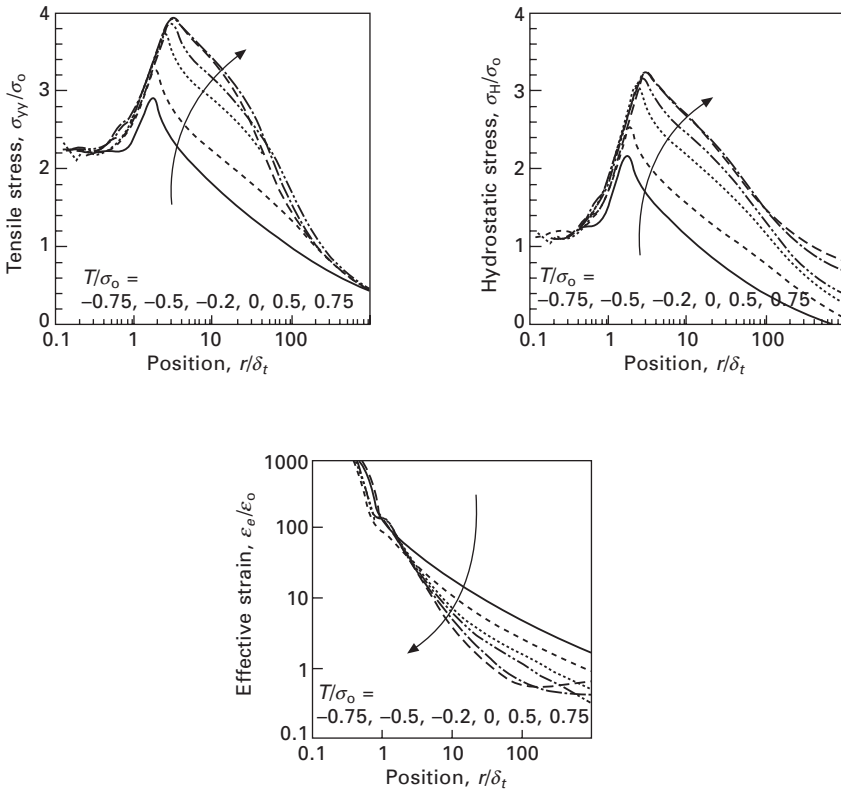
10.8 Large deformation (blunting predictions for hydrostatic stresses ahead of the crack tip for several different stress hardening exponents with $\varepsilon_o = 0.002$.

but tends to move the location of peak stresses toward the crack tip. Since stresses are normalized by the yield strength (defined in Equation 10.18), the ratio of elastic modulus to yield strength has a minor effect on crack tip stress fields.

10.4.2 Effect of T-stresses

For small-scale yielding contained well within an elastic K zone, it is instructive to consider the second term in the series expansion of elastic crack tip stresses. This term is affected by the overall cracked body geometry. It consists of an added stress parallel to the crack, σ_{11}, conventionally referred to as T. For plane strain this adds a σ_{33} stress equal to vT. The T stresses scale with the applied load and thus scale with K. The scaling constant depends on the cracked body geometry and can be positive or negative. The T stress for the finite deformation results described earlier was taken to be zero. The following paragraphs describe the blunted crack tip stress–strain environment for T stresses in the range $-0.75\sigma_o < T < 0.75\sigma_o$, resulting from the finite element calculations described above.

Figure 10.9 shows that positive T stresses increase both normal stresses and the hydrostatic stress ahead of the crack tip. The effect of positive T stresses is relatively small in contrast to the decrease in normal stresses and hydrostatic stress caused by negative T stresses. For a center-cracked panel with crack length to panel width ratio a/W less than 0.2, the T stress is given by: $T\sqrt{\pi a} = -K$. For a deeply cracked single edge cracked bend specimen

10.9 Large deformation (blunting) predictions of the effect of
T-stresses on tensile and hydrostatic stresses, for $n = 5$ and $\varepsilon_o =$
0.002. The bottom graph illustrates the effective strain ahead of the
crack tip.

with $a/W = 0.8$, a positive T stress can be developed with: $T\sqrt{\pi a} = 0.8\,K$.
For typical single edge cracked bend specimen and compact specimens T is
approximately zero. Shallow cracks in general have negative T stresses on
the order of $T\sqrt{\pi a} = -0.5K$ or less.

The utility of T in approximating the effects of specimen geometry on near
crack tip stresses is limited to small-scale yielding. With larger extents of
plastic deformation direct calculations are necessary. However, the blunted
crack tip stress field for $T = 0$ is a reasonable approximation for significant
amounts of plasticity in typical single edge cracked bend specimen and
compact specimens; that is, when the plastic zone encompasses a significant
portion of the remaining ligament, the fields likely tend toward the $T = 0$
fields.

10.4.3 Scaling of the crack tip opening displacement and maximum stresses with hardening exponents

Figure 10.10 summarizes the pre-factors associated with crack opening displacements that arise from dependencies on the hardening exponent, n, and the initial yield strain, ε_o. The dominant effect relates to the level of hardening. The dashed line in the crack opening results reflects a numerical fit to the finite element results and is given by:

$$f(n) = \frac{0.77}{1.22 + 11.63n^{1.5}} \qquad\qquad [10.20]$$
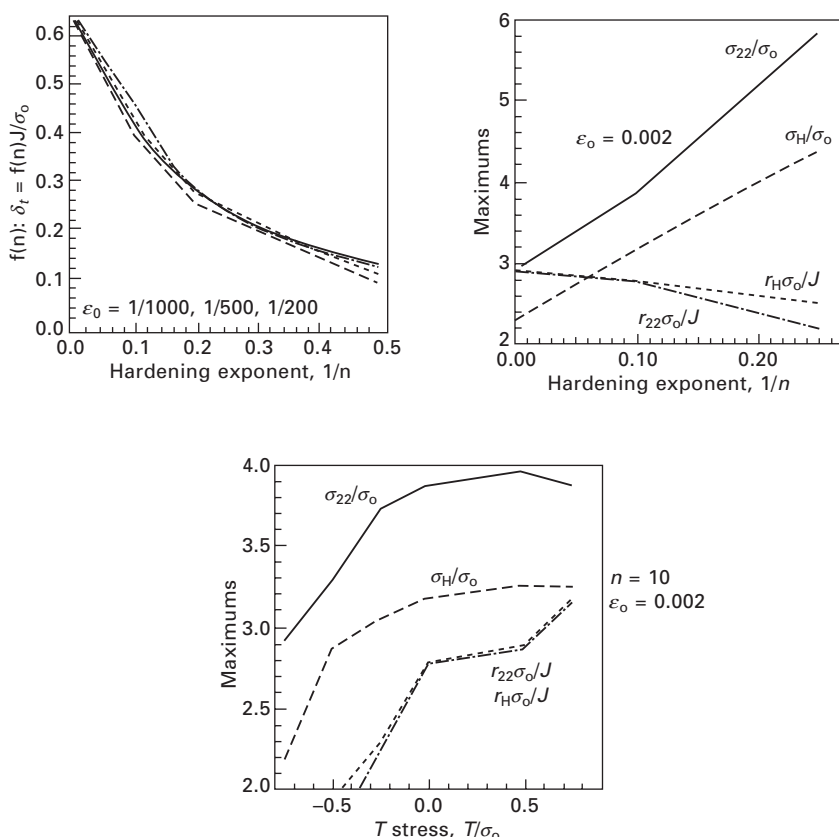
10.10 Large deformation (blunting) predictions: (top left) crack tip opening as a function of hardening exponent and yield strain: the latter has little effect; (top right) maximum tensile and hydrostatic stresses, and the radical location of the maximum, for various hardening exponents and $\varepsilon_o = 0.002$; (bottom) maximum direct stress and location of the maximum for various T-stresses, for $n = 10$ and $\varepsilon_o = 0.002$.

This can be used to estimate the crack tip opening displacement as a function of hardening exponent. Figure 10.10 also illustrates the maximum tensile stress and maximum hydrostatic stresses as a function of hardening exponent, along with the distance from the crack tip at which the maximum occurs. Decreases in hardening (associated with increasing n) cause decreases in the maximum, and push the location of the maximum slightly further from the crack tip. The effects of T-stress are also shown: negative T-stresses decrease the maximum and push its location closer to the crack tip.

10.5   Application of crack tip fields and additional considerations

10.5.1 Application of crack tip fields to gain insight into cracking mechanisms

Blunted crack tip stress–strain fields in Figs 10.6–10.10 were calculated for small scale yielding conditions. The plastic zone size is about 10% of the K zone. However, these fields persist for larger-scale yielding provided that the crack opening, δ_t, remains small compared with other specimen dimensions. The question of what is small depends on both the degree of strain hardening and overall geometry of the cracked body. Calculations and fracture toughness tests indicate that the characteristic blunted crack tip stress/strain environment is a useful approximation when the limiting dimensions of a crack body are greater than about $(10–30)J/\sigma_o$. When the thickness meets these values it is reasonable to assume near tip plane strain conditions. The lower value is appropriate to the onset of ductile tearing while the larger value is appropriate to cleavage fracture particularly in ferritic steels. As a practical matter, that is for n of 0.2 or less, assuming a characteristic blunted crack tip stress–strain environment is reasonable when limiting cracked body dimensions are greater than $(20 – 100)\delta_t$.

A very large degree of strain hardening in the range of $n = 2$ is usually the province of low strength alloys where the ratio of ultimate tensile strength to yield strength is on the order of 3, such as austenitic stainless steels and low strength nickel–base alloys (e.g. Alloy 600, Alloy 690). From Fig. 10.2 it is seen very high strain hardening, $n = 2$, leads to a normal stress that steadily increases as the crack tip is approached, in contrast to lower hardening results which reach a peak value near $r \approx 3\,\delta_t$. The hydrostatic stress does peak near $r \approx 3\,\delta_t$ but the peak is relatively broad and maintains a high value over a considerable distance ahead of the crack tip. This has important implications for hydrogen embrittlement problems, where the amount of stored hydrogen scales exponentially with the hydrostatic stress.

The above discussion is predicated on cracked body geometries of moderate to relatively high constraint such as a thick double edge cracked panel, single

edge cracked bar or a compact toughness specimen. A center-cracked panel, even with a thickness sufficient to make a plane strain assumption reasonable, is an example of a low constraint configuration. Constraint in this context is taken as an elevation of the perfectly plastic collapse load due to geometrical effects. The rigid plastic slip line field for the thick center cracked panel is simply 45° lines emanating from the crack tips. In materials with moderate toughness and low strain hardening, ductile tearing often develops as shear failure along these slip lines. In the absence of strain hardening there is no unique crack tip stress field. Even with some degree of stain hardening, low constraint specimens of this type represent a substantial challenge to the concept of a characteristic blunted crack tip stress/strain environment.

While this challenge can be avoided in testing through use of other specimen geometries it cannot be avoided in the analysis of engineering structures. For the onset of ductile tearing modes of fracture, test and calculations indicate that it is sufficient to adopt more stringent limitations on the size of limiting crack body dimensions relative to δ_t. A factor of about 5 relative to the above quoted size requirements appears reasonable. For fracture modes, such as cleavage, where a weak link approach is reasonable and both the magnitude of peak stresses and the size scale over which these stresses occur is an important consideration, other approaches are needed to approximate the effects of low constraint geometries.

The concept of a characteristic blunted crack tip stress/strain environment can provide useful insights to modeling of crack advance mechanisms and criteria. One example is a criterion for cleavage fracture that requires a high normal stress acting over a significant volume of material. A Weibull weak link approach predicts that the probability of fracture, S, is given by:

$$S = 1 - \exp\left[-cV\sigma^m\right] \tag{10.21}$$

where σ is the local stress level and V is the volume over which it acts. The terms c and m are constants. With the concept of a characteristic crack tip stress field, the stress is identified as the near peak tensile stress σ_{22} that acts over a volume of $V = \alpha B \delta_t$, where α is a constant and b is the thickness. The crack opening is proportional to J even for substantial levels of plastic deformation and for small scale yielding the crack opening is proportional to K^2. The probability of fracture then becomes:

$$S = 1 - \exp\left[-c(\alpha B \sigma^m)^2\right] \tag{10.22}$$

The near peak stress is not a function of J but the scale over which it occurs does depend on J. The above equation expresses the probability of fracture as a Weibull function and equivalently provides the cumulative distribution of cleavage fracture toughness J values. The Weibull slope is generally ~2. For small scale yielding the Weibull slope for fracture toughness expressed as K_{IC} is ~4. For a given probability of fracture, say 0.5, the product of b

and δ_t^2 must be constant. Thus the median, 50th percentile, cleavage fracture toughness for different thickness specimens must ratio according to $\sqrt{B}$ for toughness expressed as J_C and $B^{1/4}$ for toughness expressed as K_{IC}. Median cleavage fracture toughness decreases as B increases. Extensive fracture toughness testing of ferritic steels over the past 25 years is in agreement with the above development provided limiting specimen dimensions are greater than $30J/\sigma_o$.

10.5.2 Stationary vs growing cracks and crack growth thresholds

Environmentally assisted cracking is most often rate-dependent, due to the interactions between crack tip fields and species transport/reaction kinetics. A central challenge is the identification of the threshold K_{IC}^{th} for the onset of crack growth, i.e. the transition from a stationary to a growing crack (or vice versa). To contextualize the ensuing discussion regarding differences between stationary and growing cracks, it may be helpful to keep in mind two common approaches to determining the threshold K_{IC}^{th}.

In the first approach, one utilizes a fracture specimen whose K (or J) parameter decreases with crack length, after loading (presumably quickly) to a high K (or J) level followed by stable sub-critical crack growth. The K at which the crack stops growing is the arrest K for environmental crack growth: the arrest K is reached from a growing crack state, and hence, one requires the crack tip fields for a growing crack to evaluate cracking mechanisms (hydrogen concentrations, particle fracture, etc.). In the second approach, one slowly and continuously increases the applied K (or J) value under displacement control with different loading rates. The K at which crack growth begins typically depends on the loading rate. Below a critical loading rate, the K at which crack growth begins should remain constant: this would be the threshold for the onset of environmentally assisted crack growth starting from a blunted crack, and one requires the crack tip fields for a stationary crack to evaluate growth mechanisms.

For highly susceptible materials with reasonably fast environmental growth rates, the threshold values obtained from these two approaches are typically observed experimentally to be close to one another. For materials with low susceptibility with slow environmental growth rates, the two thresholds likely are not in agreement[7]. Aside from (or on top of) interactions between crack growth and transport/reaction kinetics, one possible difference between the two thresholds is the difference in crack tip fields between stationary and growing cracks.

Figure 10.11 illustrates a comparison between the tensile and hydrostatic stress distributions for a stationary crack and a crack growing at steady state, based on small deformation analyses. This comparison is based on finite
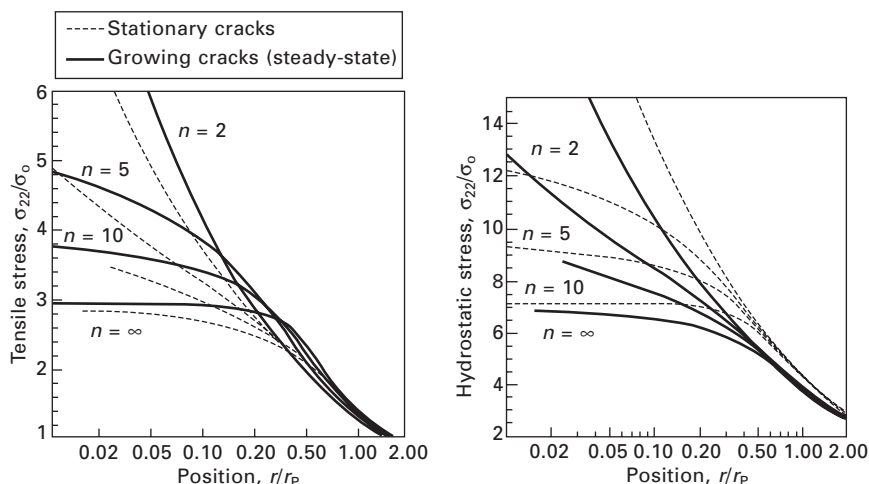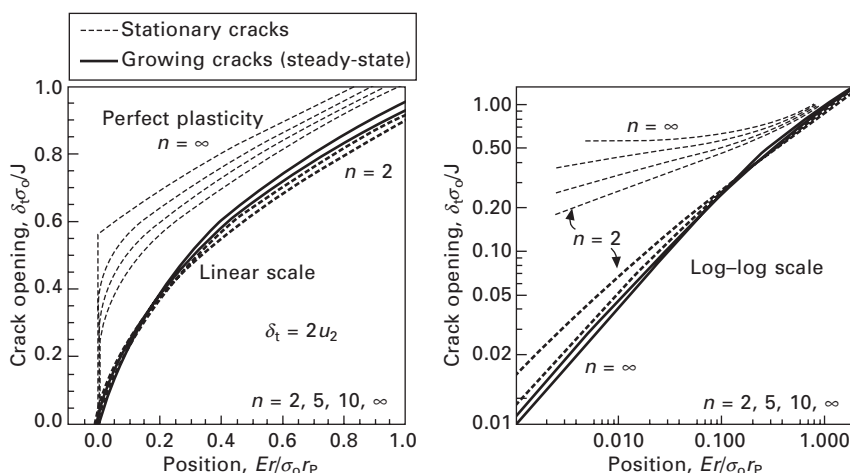
10.11 A comparison of crack tip stress distributions for stationary (dashed lines) and cracks growing at steady state (solid lines) for various hardening exponents and ε_o = 0.002.

element calculations conducted for this chapter. The results for stationary cracks are close to the HRR fields, with some differences arising due to the incompressibility constraint invoked in the HRR fields [9, 11] (which is not invoked in these finite element computations). The value for tensile stress for the perfectly plastic material ($n = \infty$) at the crack tip (i.e. $\sigma_{22}/\sigma_o \approx$ 3) is the same as predicted in an analytical solution by Drugan *et al*. [20]. Note that significant differences arise as the degree of hardening increases. Also note that the tensile stresses are larger for the growing crack, while hydrostatic stresses are larger for the stationary crack. This may have important implications for hydrogen embrittlement.

Comprehensive solutions for a growing crack with large deformation (blunting) are not readily available, although limited results are included in [13, 21, 22]). It is perhaps reasonable to anticipate similar differences between stationary and growing cracks as implied by small deformation results.

Figure 10.12 illustrates a comparison between the crack opening displacements for small deformation analyses of a growing crack and a stationary crack (the latter given by the HRR solutions). Figure 10.12 illustrates that growing cracks are much sharper than stationary cracks, with openings 10–20 smaller than stationary cracks for locations less than 1% of the plastic zone size from the tip.

A comparison of the opening results in Fig. 10.12 (for small deformation) and those in Fig. 10.10 (for large deformation) is somewhat obfuscated by the presence of the notch tip required for finite deformation simulations.

10.12 A comparison of crack tip opening distributions for stationary (dashed lines) and cracks growing at a steady state (solid lines) for various hardening: the normalization accounts for all values of $\varepsilon_o = \sigma_o /E$.

However, one approach is to evaluate the small deformation displacements at a position equivalent to the distance to the peak stress in finite deformation simulations, i.e. $r \approx 2J/\sigma_o$ (see Fig. 10.10). At this distance, finite deformation effects are active but the notch radius is inconsequential due to large blunting deformations. This distance corresponds to $r/r_P \sim \sigma_0/(3\pi E)$, which is at the extreme left (minimum) of Fig. 10.12. Comparing the intercepts of the opening at $r/r_P \sim 0.001$ with the results in Fig. 10.10, it is clear that the finite deformation effects have a small impact on crack opening for stationary cracks, unless one uses the small deformation results for distances within the blunting region. The implication is that the reduction in crack opening due to the presence of a growing crack is a factor of 10–20 even for large deformation simulations. Such opening differences are potentially very important for environmental transport phenomena in the wake of the crack that drives hydrogen embrittlement effects.

10.5.3 Crack tip stress elevation beyond conventional plasticity predictions

The implications of crack tip stresses on hydrogen uptake are of central interesting in environmentally assisted cracking, particularly so since the hydrogen concentration scales exponentially with the hydrostatic stress. Conventional plasticity simulations such as those summarized here predict relatively modest stresses in that they lead to relatively low hydrogen

concentrations. In a strongly related vein, the prediction of modest stresses of $(3-5)\sigma_o$ makes it difficult to rationalize the occurrence of brittle failures in the presence of plastic flow, since they presumably imply bond rupture occurring at much higher stresses ($\sim 10\sigma_o$).

As a result, there have been many attempts to model mechanisms that lead to higher stresses than those predicted by conventional plasticity. These broadly fall into two categories: (i) the inclusion of discrete features, such as dislocations [4–6, 23, 24], dislocation-free zones (e.g. [25, 26]), etc., and (ii) the use of non-local plasticity theories which introduce elevated flow stresses through Taylor-enhanced strain hardening (e.g. [27–33]). The first of these approaches is entirely different from continuum simulations of the character summarized here, as it requires additional microstructural details that are likely highly specific to a given material and cracking mechanism. The second approach bears commenting – continuum predictions of crack tip stresses via non-local plasticity [27–33].

A consensus has yet to emerge regarding a preferred constitutive description that incorporates length-scale effects. Regardless, the details of the so-called length-scale plasticity constitutive law are likely beside the point at this stage: all theories predict elevated hardening in the presence of strain gradients (their basic intent), and all theories require constitutive parameters that are difficult to identify experimentally: namely, length-scale parameters that depend on the material microstructure and control the strength of the strain gradient effect. The current greatest hope for determining these length-scales is nanoindentation experiments (e.g. [34–37]).

The central issue in application of strain gradient plasticity (SGP) theories is whether or not SGP effects persist over a length-scale for which continuum theories can be reasonably applied. Recent small-deformation simulations for SGP over a broad range of applied stress intensity factors and macroscopic plasticity parameters (i.e. yield stress and hardening exponent) have illustrated that crack tip stress elevation (over that predicted by the HRR fields) persists to a distance given by [33]:

$$r^* = c\frac{K_I \sqrt{l}}{\sigma_Y} \qquad\qquad [10.23]$$

where l is the material length-scale parameter (determined via indentation tests), and c is a dimensionless constant that depends on the constitutive formulation (specifically, on different length-scales associated with different types of strain gradients). Here, r^* refers to the distance over which the stresses are at least twice the HRR solutions: interestingly, the role of the hardening exponent is completely captured by reference to the HRR solutions, such that the above is reasonably accurate for any hardening exponent. Clearly, the most relevant materials for which SGP effects may play a significant role are those with relative low yield stress and at relatively large applied

stress intensity factors. The most optimistic estimates of c (which produce the largest regions of SGP effects) place it only at about ~0.02 [33].

The difficulty in applying SGP to hydrogen cracking lies in the relatively small estimates of the material length-scale, l, that are appropriate for these theories: for soft materials free of microstructural features (e.g. annealed copper), $l \sim 1\,\mu m$ [34]. For an alloy with fine microstructure, l is much smaller, in the range of 100–250 nm [37]. To understand the central concern for applying SGP theory, consider a relatively soft steel alloy with $\sigma_o = 500$ MPa, loaded to a relatively high state, e.g. $K_I \sim 70\,\mathrm{MPa}\sqrt{m}$. Taking the length-scale to be 0.1–0.5 μm, this suggests that SGP effects persist to 0.8 to 2 μm. One the one hand, this is perhaps acceptable, being larger than the underlying length-scale, such that it is reasonable to neglect explicit reference to microstructural features. On the other, it is problematic since it is smaller than the size of region impact by finite deformation, predicted via Fig. 10.10 to be ~3–5 μm. This emphasizes the importance of conducting finite-deformation simulations with SGP: initial results suggest that finite deformation effects on SGP predictions are not dramatic [30]. Of course, applied stress intensities relevant to hydrogen embrittlement can be an order of magnitude lower, and yield stresses for relevant materials may be twice as high. This would imply SGP effects persist to only 40–100 nm, which is clearly problematic, as it is difficult to rationalize the neglect of specific microstructural features on this length scale.

As such, we anticipate that crack tip simulations to rationalize high stresses will track towards explicit reference to material microstructure, such as combining discrete dislocation simulations [4–6, 24] with specific features that alter plasticity (such as hard inclusions or local grain orientation variations). Clearly, however, SGP approaches cannot be ruled out until the scaling that emerges with finite deformation is fully quantified.

10.5.4 Cohesive zone modeling

As a final note on crack tip stresses, it is worth mentioning the advent of cohesive zone models that explicitly predict crack growth as a natural consequence of loading and deformation, without invoking an artificial growth criterion based on singular fields [38–43]. Perhaps the greatest opportunity for these models is created by their ability to cleanly couple distinct treatments of the role of an intrinsic toughness (i.e. the area under an atomic force-separation description) and plastic deformation. This approach is particularly attractive for hydrogen embrittlement problems, for which there is reason to believe that the presence of hydrogen impacts the cohesive strength of atomic bonds (regardless of its role in altering the nature of plastic deformation). One can couple first-principle calculations of the effects of hydrogen on bond rupture to conventional plasticity descriptions [40], or

simply describe an intrinsic toughness that is a function of hydrogen uptake [41–43]. The details as to how cohesive tractions should be altered to account for the presence of hydrogen (without improperly impacting plasticity) are still emerging, and beyond the scope of this review chapter. Suffice it to say, cohesive zone models have shown great promise in predicting stress intensity thresholds and crack growth rates, and their application in this arena will undoubtedly grow.

## 10.6   Stresses around dislocations and inclusions

10.6.1 Dislocations

The stresses and strain energies associated with dislocations (lattice defects) play an integral role in assessing the degree of hydrogen storage and trapping. This section is meant merely to provide a handy reference for classical elasticity solutions (for isotropic media). More complete details are available elsewhere [44, 45]. The stress fields surrounding pure screw and pure edge dislocations, as illustrated in Fig. 10.13, are summarized in Table 10.2, along with the associated strain energy (per unit length of the dislocation line). In these results, G is the shear modulus of the material, v is the Poisson ratio, R is the distance to a stress-free boundary, and b is the Burgers vector of the dislocation. The parameter r_0 is the minimum distance from the dislocation for which the elasticity solution is presumed valid.

   Note that the energy associated with the dislocation scales with size of the region over which energy is calculated, R: in reality, the energy associated with distant positions is canceled due to that associated with image stresses. For practical reasons, the size of the stressed zone, R, and associated strain energy is defined as the distance between the dislocation and a free surface (for isolated dislocations) or as one half of the average distance between dislocations (for multiple dislocations) [44].

   Also, it should be noted that the linear elasticity solution breaks down for positions close to the dislocation core, for which the energy should be strictly determined from a detailed atomistic analysis of the disturbed lattice. A common rule of thumb, based on analysis of a periodic lattice, is to define the elasticity valid for $r > b/4$ [44].

   The fact that dislocation stress fields based on linear elasticity are reasonably accurate (subject to the limitations discussed above) enables one to generate an infinite array of solutions for multiple dislocation arrangements via superposition. Here, one of the myriad of solutions is summarized, that for a continuous pile-up of edge dislocations near an obstacle. The dislocation distribution is assumed to be described by a continuous dislocation density, which defines a displacement discontinuity along the plane of the pile-up: in essence, the dislocation pile-up is a slit that cannot support shear stress
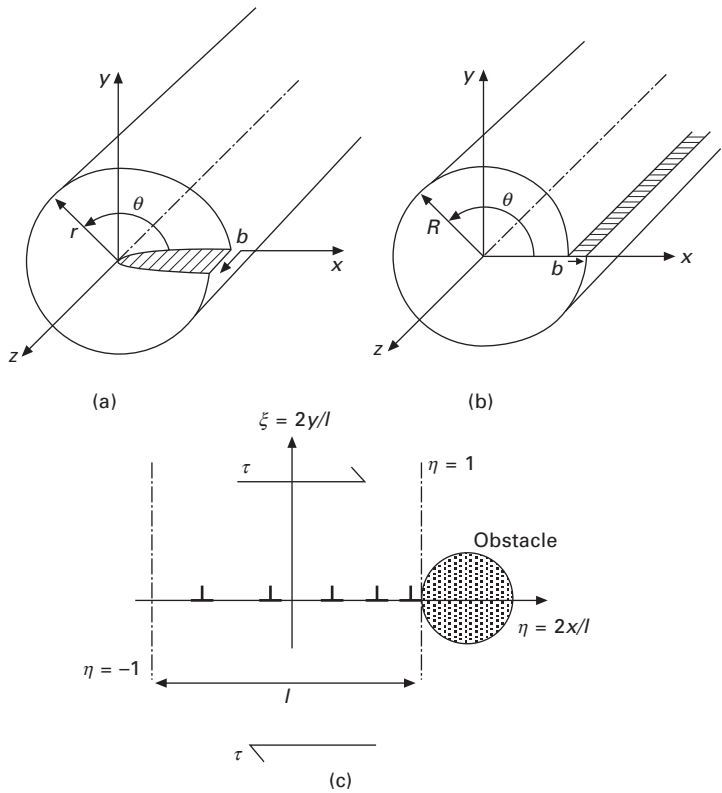
10.13 Schematic illustration of dislocations and coordinator systems used in the analysis: (a) screw dislocation, (b) edge dislocation, (c) array of edge dislocations trapped against an obstacle for material subjected to shear stress.

Table 10.2 Summary of stress fields and energies associated with dislocations

Screw dislocation	Edge dislocation
$\sigma_{xz} = \dfrac{-Gb}{2\pi}\dfrac{\sin\theta}{r} = \dfrac{-Gb}{2\pi}\left(\dfrac{y}{x^2+y^2}\right)$	$\sigma_{xx} = \dfrac{-Gb}{2\pi(1-v)}\left[\dfrac{3x^2+y^2}{(x^2+y^2)^2}\right]$
	$\sigma_{yy} = \dfrac{Gb\cdot y}{2\pi(1-v)}\left[\dfrac{x^2-y^2}{(x^2+y^2)^2}\right]$
$\sigma_{yz} = \dfrac{-Gb}{2\pi}\dfrac{\cos\theta}{r} = \dfrac{-Gb}{2\pi}\left(\dfrac{x}{x^2+y^2}\right)$	$\sigma_{xy} = \dfrac{Gb\cdot x}{2\pi(1-v)}\left[\dfrac{x^2-y^2}{(x^2+y^2)^2}\right]$
$E_{screw} = \dfrac{Gb^2}{4\pi}\ln\dfrac{R}{r_a}$	$E_{edge} = \dfrac{Gb^2}{4\pi(1-v)}\ln\dfrac{R}{r_o}$

$$E_{mixed} = \frac{Gb^2}{4\pi(1-v)}(1-v\cos^2\beta)\ln\frac{R}{r_a}$$

but can support stresses normal to the pile-up plane. In this approach, the dislocation pile-up is effectively the same as a shear crack.

In the analysis of the pile-up (illustrated in Fig. 10.13), the coordinates are normalized by the length of the pile-up, l, such that the pile-up runs from $-1 \leq \eta = 2x/l \leq 1$. The length of the pile-up is dictated by the total number of dislocations, N, and the applied shear stress, τ:

$$l = \frac{Nb}{\pi(1-v)}\left(\frac{G}{\tau}\right) \qquad [10.24]$$

The dislocation distribution – in this case a linear density (dislocations per unit length along the pile-up) – is given by:

$$\rho(\eta) = \frac{2(1-v)}{b}\left(\frac{\tau}{G}\right)\sqrt{\frac{1+\eta}{1-\eta}} \qquad [10.25]$$

In the analysis, the dislocation density at the trailing edge $\eta = 1$ is set to zero as a boundary condition. The stress field surrounding the dislocation pile-up is given by:

$$\frac{\sigma_{xx}}{\tau} = -1 \ -\alpha\{\zeta\sin\phi\,[3\,(\eta-1)^2 + \zeta^2]\}$$

$$+ \cos\phi\,[-(1+\eta)(\eta-1)^2 - 2\zeta^2(\eta-1)^2 - \zeta^4] \qquad [10.26a]$$

$$\frac{\sigma_{yy}}{\tau} = -\alpha\,\{\cos\phi\,[\zeta(\zeta^2 - (\eta-1)^2)] - 2\sin\phi\,[\zeta^2\,(\eta-1)]\} \qquad [10.26b]$$

$$\frac{\sigma_{xy}}{\tau} = -\alpha\,\{\cos\phi\,[5(\eta-1)^2 + 3\zeta^2] - 2\sin\phi\,[(1+\eta)(\eta-1)^3$$

$$- 2\zeta^2\,(\eta-1)(2\eta-1) + \zeta^4]\} \qquad [10.26c]$$

where $\zeta = 2y/l$ and the additional coordinate parameters are given by:

$$\phi = 2\tan^{-1}\left(\frac{2\zeta}{\eta^2 + \zeta^2 - 1}\right) \qquad [10.26d]$$

$$\alpha = \frac{[(\eta^2 + \zeta^2 - 1)^2 + 4\zeta^2]^{1/4}}{\sqrt{(\eta+1)^2 + \zeta^2}\,[(\eta-1)^2 + \zeta^2]^2} \qquad [10.26e]$$

It should be noted that ϕ should be defined to have the proper sign for each quadrant (i.e. positive above the pile-up and negative below).

These solutions can be coded in symbolic mathematics software to plot contours of stresses and strain energy. Figure 10.14 illustrates the distribution of hydrostatic stresses around the pile-up, and the strain energy stored in the disturbed lattice. The hydrostatic stress is dominated by the σ_{xx} stress, which is compressive above the dislocation array, and tensile beneath it.
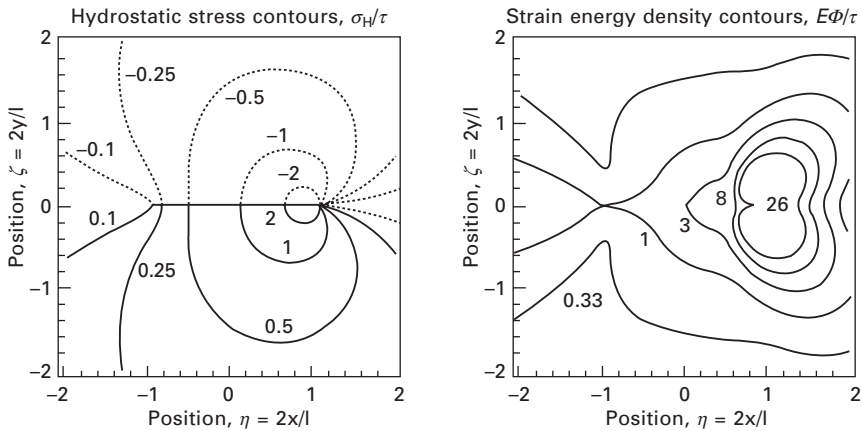
10.14 Contours of hydrostatic stress and strain energy density surrounding an edge-dislocation pile-up. Contours below the crack are for $\sigma_H/\tau = 0.1, 0.5, 1, 1.5, 2$. Energy contours for $EW/\tau = 0.33, 1, 3, 8.7, 26$.

10.6.2 Inclusions

The stress and deformation fields in and around an ellipsoidal elastic inclusion embedded in an infinite elastic matrix was solved in completely general terms by Eshelby [46]: this famous paper (often credited as being the most cited paper of all time in mechanics) describes the entire solution in closed form for an ellipsoid of arbitrary dimensions subjected to an arbitrary spatially uniform 'transformation strain' tensor applied to the inclusion. (This transformation strain can be thought of as the superposition of the inclusion deformation induced by remote loading and thermal strains or those associated with phase transformation.) Surprisingly, regardless of the aspect ratio of the inclusion or the remote loading conditions, the stress/strain state in the inclusion is spatially uniform.

While the general solution can be obtained in closed-form, the procedure involves cumbersome linear algebra associated with fourth-order tensors [10, 45]. Here, we present simplified solutions for a spherical inclusion in matrix that is subjected to remote uniform stress in one direction, as illustrated in Fig. 10.15. Both elastic mismatch (E_i = modulus of the inclusion and E_m = modulus of the matrix), and thermal expansion mismatch are included, with fixed Poisson ratios to simplify the results: $v_i = 0.1$ and $v_i = 0.35$. Here, $\Delta\alpha = \alpha_m - \alpha_i$ is the difference in the coefficients of thermal expansion; ΔT is the change in temperature of the system, defined relative to the temperature for which there are no thermal strains in either the inclusion or matrix. (For simplicity, it is assumed that both the inclusion and matrix have the same reference temperature.) The hydrostatic stress in the inclusion is given by
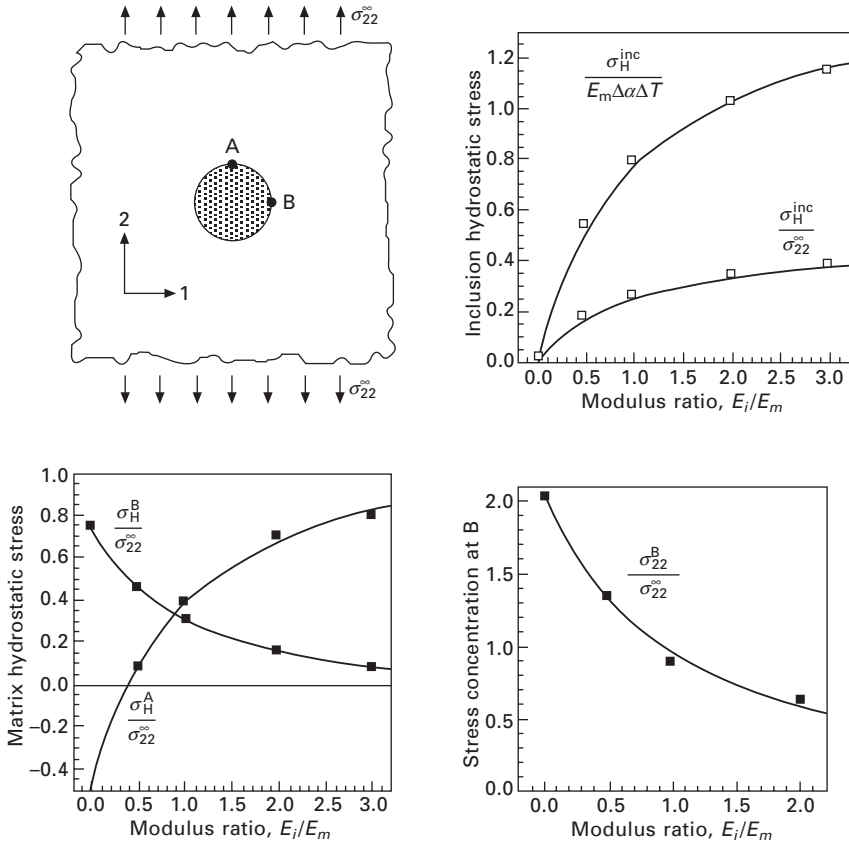
10.15 Summary of key results for a spherical elastic inclusion embedded in an elastic matrix: the total stress arising from thermal mismatch and remote tension can be superimposed. The hydrostatic stress in the inclusion is spatially uniform. The hydrostatic stress in the matrix varies as a function of positions.

the superposition of stresses arising from thermal mismatch and remote tension:

$$\frac{\sigma_H^i}{E_i} \cong \frac{E_m}{(E_\blacksquare + E_m)}\left(\frac{3}{2}\Delta\alpha\Delta T + \frac{1}{2}\varepsilon_{22}^\infty\right) \qquad [10.27a]$$

where ε_{22}^∞ is the remote strain at infinity (i.e. the strain caused by the applied tension). The form of this equation is identical to that obtained via Eshelby's analysis, and as such is asymptotically exact for all range of mismatch: the pre-factors in the numerator and denominator are weak functions of the Poisson ratio. At the risk of raising the hackles of our mentors, we avoided the cumbersome algebra by determining the pre-factors via fitting to FEA

results: in this regard, the results present here are approximate, and one will obtain very slightly different pre-factors when executing the full Eshelby solution.

The hydrostatic stresses in the matrix at points A and B in Fig. 10.15 (A is directly above the inclusion in the direction of tension, while B is adjacent to the inclusion) are given by:

$$\frac{\sigma_H^i}{E_i} \cong \frac{E_m}{(E_\blacksquare + E_m)}\left[\frac{3}{2}\Delta\alpha\Delta T + \left(1.26 - \frac{E_m}{2E_i}\right)\varepsilon_{22}^\infty\right] \qquad [10.27b]$$

$$\frac{\sigma_H^i}{E_i} \cong \frac{E_m}{(E_\blacksquare + E_m)}\left[\frac{3}{2}\Delta\alpha\Delta T + \left(0.75\frac{E_m}{E_i} - 0.14\right)\varepsilon_{22}^\infty\right] \qquad [10.27c]$$

These stresses represent the maximum hydrostatic stresses in the matrix: stresses decay away from the interface according to $(a/r)^3$, where a is the inclusion radius. Finally, the tensile stress concentration in the matrix at the side of the particle is given by:

$$\frac{\sigma_{22}^B}{E_m\varepsilon_{22}^\infty} \cong \frac{E_m}{(E_\blacksquare + E_m)}\left[2.05 - 0.14\frac{E_i}{E_m}\right] \qquad [10.27d]$$

10.7   Conclusions

- In order to evaluate the plausibility or potential impact of stress-influenced cracking mechanisms, including those involving hydrogen, one must be able to quantify two key aspects of the stresses and deformation near the crack tip: the physical length-scale over which crack tip stresses are elevated, and the degree of stress elevation. The present chapter provides a summary of classical continuum simulations of crack tip fields based on conventional elastic and elastic-plastic crack tip fields.
- Straightforward empirical relationships (based on fits to finite element solutions) greatly facilitate the estimate of crack tip stress elevation and the size of the elevated stress region in terms of the yield strain and strain hardening exponent. Similarly, condensed results are presented for stresses near dislocation pile-ups and inclusions. These results enable researchers to quickly evaluate the extent and severity of stress-assisted hydrogen uptake, across a broad class of materials with various types of plastic response and at a broad range of applied loading parameters. The impact of non-singular T-stresses is also elucidated using several example cases.
- This chapter provides a comparison of fields for stationary cracks and cracks growing at steady state; while the differences between stresses are relatively minor, there are dramatic differences in the crack opening profiles resulting from these two types of analyses. This could have

important implications for hydrogen embrittlement problems, where environmental transport in the wake of the crack is affected by the length-scales associated with crack openings.

- Recent simulations of crack tip behavior that account for elevated hardening levels due to the presence of strain gradients, microstructural features and cohesive behaviors suggest that classical continuum theories may not accurately predict stresses near crack tip, in particular near local microstructural features. The present summary serves as an entry point to assessing the potential of these models, by enabling one to identify the length-scales over which discrete features or gradient effects should be included.

10.8   Acknowledgement

10.9   References

[1] Flouriot, S., Forest, S., Calletaud, G., Koster, A., Remy, L, Burgardt, B., Gros, V., Mosset, S. and Delautre, J. (2003) Strain localization at the crack tip in single crystal CTE specimens under monotonic loading: 3D finite element analyses and application to nickel-based superalloys, *International Journal of Fracture*, **124**, 43–77.

[2] Rice, J.R. (1992) Dislocation nucleation from a crack tip: an analysis based on the Peierls concept, *Journal of the Mechanics and Physics of Solids*, **40**, 239–271.

[3] Needleman, A. and Tvergaard, V. (1987) An analysis of ductile rupture modes at a crack tip, *Journal of the Mechanics and Physics of Solids*, **35**, 151–183.

[4] Van der Giessen, E., Desphande, V.S., Cleveringa, H.H.M. and Needleman, A. (2001) Discrete dislocation plasticity and crack tip fields in single crystals, *Journal of the Mechanics and Physics of Solids*, **49**, 2133–2153.

[5] Cleveringa, H.H.M., Van der Giessen, E. and Needleman, A. (2000) A discrete dislocation analysis of mode I crack growth, *Journal of the Mechanics and Physics of Solids*, **48**, 1133–1157.

[6] Chakravarthy, S. and Curtin, W.A., (2010) Origin of plasticity length-scale effects in fracture, *Physical Review Letters*, **105**, #115502.

[7] McMeeking, R.M. and Rice, J.R. (1975) Finite-element formulations for problems of large elastic-plastic deformation, *International Journal of Solids and Structures*, **11**, 601–616.

[8] Bower, A.F. (2010) *Applied Mechanics of Solids*, CRC Press, Boca Raton, FL (USA).

[9] Hutchinson, J.W. (1968) Singular behavior at the tip of a crack in a hardening material, *Journal of the Mechanics and Physics of Solids*, **16**, 13–31.

[10] Gangloff, R.P. (2003) 'Hydrogen assisted cracking in high strength alloys,' in *Comprehensive Structural Integrity*, Milne, I., Ritchie, R.O. and Karihaloo, K, Eds. in Chief, Petit, J. and Scott, P., Vol. Eds., Vol, 6, Elsevier Science, New York, NY, pp. 31–101.

[11] Rice, J.R. and Rosengren, G.F. (1968) Plane strain deformation near a crack tip in a power-law hardening material, *Journal of the Mechanics and Physics of Solids*, **16**, 1–12.

[12] Anderson, T.L. (1995) *Fracture Mechanics: Fundamentals and applications*, CRC Press, Boca Raton, FL (USA).

[13] McMeeking, R.M. (1977) Finite deformation analysis of crack-tip opening in elastic-plastic materials and implications for fracture, *Journal of the Mechanics and Physics of Solids*, **25**, 357–381.

[14] Rice, J.R. (1968) A path independent integral and approximate analysis of strain concentration by notches and cracks, *Journal of Applied Mechanics*, **35**, 379–386.

[15] Rice, J.R. (1968) 'Mathematical analysis in the mechanics of fracture,' *Fracture: An Advanced Treatise*, vol. II, ed. Liebowitz, H., Academic Press, New York, pp. 191–311.

[16] Carka, D., Mear, M.E. and Landis, C.M. (2011) 'The Dirichlet-to-Neumann map for two-dimensional crack problems,' *Computer Methods in Applied Mechanics and Engineering*, **200**, 1263–1271.

[17] Givoli, D. and Keller, J.B. (1989) A finite element method for large domains, *Computer Methods in Applied Mechanics and Engineering*, **76**, 41–66.

[18] Givoli, D. and Rivkin, L. (1993) The DtN finite-element method for elastic domains with cracks and re-entrant corners, *Computers and Structures*, **49**, 633–642.

[19] Hilton, P.D. and Hutchinson, J.W. (1971) Plastic intensity factors for cracked plates, *Engineering Fracture Mechanics*, **3**, 435–451.

[20] Drugan, W.J., Rice, J.R. and Sham, T.-L. (1982) Asymptotic analysis of growing plate strain tensile cracks in elastic-ideally plastic solids, *Journal of the Mechanics and Physics of Solids*, **30**, 447–473.

[21] Xia, L., Shih, C.F. and Hutchinson, J.W. (1995) A computational approach to ductile crack growth under large scale yielding conditions, *Journal of the Mechanics and Physics of Solids*, **43**, 389–413.

[22] O'Dowd, N.P., Shih, C.F. and Dodds, R.H. (1995) The role geometry and crack growth on constraint and implications for ductile/brittle fracture, *Constraint Effects in Fracture Theory and Applications*: 2nd Volume, ASTM STP 1244, Kirk, M. and Bakker, A. editors, ASTM, Philadelphia, 1995.

[23] Lii, M.-J., Chen, X.-F., Katz, Y. and Gerberich, W.W. (1990) Dislocation modeling and acoustic emission observation of alternating ductile/brittle events in Fe–3wt%–Si crystals, *Acta Metallurgica et Materialia*, **38**, 2435–2453.

[24] Song, J. and Curtin, W.A. (2011) A nanoscale mechanism of hydrogen embrittlement in metals, *Acta Materialia*, **59**, 1557–1569.

[25] Suo, Z., Shih, C.F. and Varias, A.G. (1993) A theory for cleavage in the presence of plastic flow, *Acta Metallurgica et Materialia*, **41**, 1551–1557.

[26] Beltz, G.E., Rice, J.R. and Shih, C.F. (1996) A self-consistent model for cleavage in the presence of plastic flow, *Acta Materialia*, **44**, 3943–3954.

[27] Wei, Y. and Hutchinson, J.W. (1997) Steady-state crack growth and work of fracture for solids characterized by strain gradient plasticity. *Journal of the Mechanics and Physics of Solids*, **45**, 1253–1265.

[28] Chen, J.Y., Wei, Y., Huang, Y., Hutchinson, J.W. and Hwang, K.C. (1999) The crack tip fields in strain gradient plasticity: the asymptotic and numerical analyses, *Engineering Fracture Mechanics*, **64**, 625–648.

[29] Jiang, H., Huang, Y., Zhuang, Z. and Hwang, K.C. (2001) Fracture in mechanism based strain gradient plasticity, *Journal of the Mechanics and Physics of Solids*, **49**, 979–993.

[30] Hwang, K.C., Jiang, H., Huang, Y. and Gao, H. (2003) Finite deformation analysis of mechanism-based strain gradient plasticity: torsion and crack tip field, *International Journal of Plasticity*, **19**, 235–251.

[31] Wei, Y., Qui, X. and Hwang, K.C. (2004) Steady-state crack growth and fracture work based on the theory of mechanism-based strain gradient plasticity, *Engineering Fracture Mechanics*, **71**, 107–125.

[32] Qu, S., Huang, Y., Jiang, H., Liu, C., Wu, P.D. and Hwang, K.C. (2004) Fracture analysis in the conventional theory of mechanism-based strain gradient (CMSG) plasticity, *International Journal of Fracture*, **129**, 199–220.

[33] Komaragiri, U., Agnew, S.R., Gangloff, R.P. and Begley, M.R. (2008) The role of macroscopic hardening and individual length-scales on crack tip stress elevation from phenomenological strain gradient plasticity, *Journal of the Mechanics and Physics of Solids*, **56**, 3527–3540.

[34] Nix, W.D. and Gao, H. (1998) Indentation size effects in crystalline materials: a law for strain gradient plasticity, *Journal of the Mechanics and Physics of Solids*, **46**, 411–425.

[35] Swadener, J.G., George, E.P. and Pharr, G.M. (2002) The correlation of the indentation size effect measuremed with indenters of various shapes, *Journal of the Mechanics and Physics of Solids*, **50**, 681–694.

[36] Begley, M.R. and Hutchinson, J.W. (1998) The mechanics of size-dependent indentation, *Journal of the Mechanics and Physics of Solids*, **46**, 2049–2068.

[37] Ro, Y.J., Begley, M.R., Gangloff, R.P. and Agnew, S.R. (2006) Effects of aging on scale-dependent plasticity in aluminum alloy 2024, *Materials Science and Engineering A*, **435–436**, 333–342.

[38] Xu, X.P. and Needleman, A. (1994) Numerical simulations of fast crack growth in brittle solids, *Journal of the Mechanics and Physics of Solids*, **42**, 1397–1434.

[39] Remmers, J.J.C, de Borst, R. and Needleman, A. (2003) A cohesive segments method for the simulation of crack growth, *Computational Mechanics*, **31**, 69–77.

[40] Serebrinsky, S., Carter, E.A. and Ortiz, M. (2004) A quantum-mechanically informed continuum model of hydrogen embrittlement, *Journal of the Mechanics and Physics of Solids*, **52** (10), 2403–2430.

[41] Olden, V., Thaulow, C. Johnsen, R., Ostby, E. and Berstad, T. (2008) Application of hydrogen influence cohesive laws in the prediction of hydrogen induced stress cracking in 25%Cr duplex stainless steel, *Engineering Fracture Mechanics*, **75**, 2333–2351.

[42] Schieder, I., Pfuff, M. and Dietzl, W. (2008) Simulation of hydrogen assisted stress corrosion cracking using the cohesive model, *Engineering Fracture Mechanics*, **75**, 4283–4291.

[43] Olden, V., Thaulow, C. Johnsen, R., Ostby, E. and Berstad, T. (2009) Influence of hydrogen from cathodic protection on the fracture susceptibility of 25%Cr duplex stainless steel – constant load SENT testing and FE-modelling using hydrogen influence cohesive zone elements, *Engineering Fracture Mechanics*, **76**, 872–844.

[44] Hirth, J.P. and Locke, J. (1968) *Theory of Dislocations*, McGraw-Hill, New York, NY (USA).

[45] Hull, D. and Bacon, D.J. (1984) *Introduction to Dislocations*, Pergamon Press, Oxford, England.

[46] Eshelby, J.D. (1957) The determination of the elastic field of an ellipsoidal inclusion, and related problems, *Proceedings of the Royal Society of London A*, **241**, 376–396.